Università degli Studi di Ferrara

DOTTORATO DI RICERCA IN
FISICA

CICLO XXIII

COORDINATORE Prof. Filippo Frontera

K-edge Radiography and applications to Cultural Heritage

Settore Scientifico Disciplinare FIS/07

Dottorando
Dott. Albertin Fauzia

Tutori
Prof. Gambaccini Mauro
Prof. Petrucci Ferruccio

Anni 2008/2010

Contents

Introduction

The present work of thesis is focused on application of X-ray K-edge technique to paintings.
This technique allows one to achieve a topographic map of a pigment on the whole surface of the painting.
The digital acquisition of radiographic images by using monochromatic X-ray beams allows to take advantage of the sharp rise of X-ray absorption coefficient of the elements, the K-edge discontinuity.
Working at different energies, bracketing the K-edge peak, allows recognition of the target element.
The K-edge radiography facility installed at Larix Laboratory, at Department of Physics in Ferrara, consists of a quasi-monochromatic X-ray beam obtained via Bragg diffraction on a mosaic crystal from standard X-ray source.
In the first 3 chapters a description of the K-edge technique and the experimental apparatus are presented.
In chapter 4 the characterization of the monochromatic beams in the 7-40 KeV range is presented.
K-edge elemental mapping of Iron, Cobalt, Copper, Zinc, Arsenic, Cadmium and Tin, on test object and test painting, have been carried out and result is shown in chapter 5.
In the end, a transportable facility for digital radiography is presented and some radiographic analysis of works of art performed are shown.

Chapter 1

K-edge Radiography

1.1 Elemental analysis on painting layers: K-edge technique

The traditional X-ray radiography plays an important role in scientific diagnostics of cultural heritage. It can reveal execution techniques and underpaintings information. But it is based on X-ray attenuation of materials and it cannot provide analytical composition [1].
Widely used, non-invasive techniques to perform elemental analysis on painting layers are X-ray fluorescence (XRF) [2] and Particle-Induced X-ray Emission (PIXE) [3]. These techniques allow for simultaneous detection of elements on a painting but the inspection is intrinsically local and it is not designed to perform exhaustive analyses in large areas.
A topographic map of one pigment on the whole surface of a painting can be obtained with K-edge technique, originally proposed by Lehmann [4] for medical applications [7, 8] and in recent years applied to cultural heritage [9, 10].
This technique takes advantage of the sharp rise of X-ray absorption coefficient of the elements, the K-edge discontinuity.
Working at different energies, below and above the K-edge peak, allows to make recognition of the target element. Realizing two radiographies with this energy choice means maximizing the signal variation of target element while maintaining almost unchanged the response from the background.
The images are processed by Lehmann algorithm to obtain two new images: the first one giving the mass density distribution (g/cm^2) of the K-edge element while the second one giving the distribution of all other materials in the sample.
An elemental map by dual energy radiography can be obtained in a reasonable time with monochromatic X-ray beams, as produced by a synchrotron source [10]. The aim of this work is to investigate this technique using a device transportable in a museum that consists of a quasi-monochromatic X-ray source obtained via Bragg diffraction on a mosaic crystal and a standard X-ray tube.

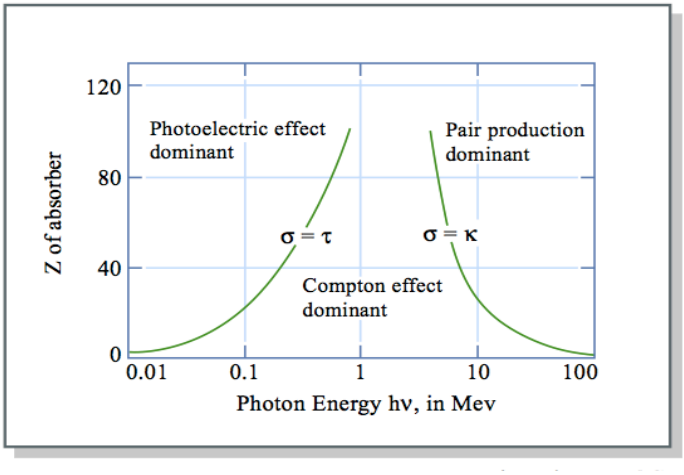

Figure 1.1: Photoelectric effect, Compton effect and pair production and their dominance at different energies and Z of absorber.

1.2 X-ray absorption in matter

In X-ray interaction with matter three process can occur, depending on X-ray energy and atomic number of the target: photoelectric absorption, Compton effect and pair production.
X-rays trasmission through a target of thickness x is expressed by

$$I = I_0 e^{-\mu x} \tag{1.1}$$

where I is the number of photons emerging from the target, I_0 the number of photons impinging on the target and μ is the total *linear attenuation coefficient*.
Linear attenuation coefficient μ represents the sum of the coefficients related to the three different process: τ for photoelectric, σ for Compton and κ for pair production.

$$\mu = \tau + \sigma + \kappa \tag{1.2}$$

The three different process and their dominance are shown in Fig.1.1 as a function of photon energy and Z of the absorber.
As shown at low energy (1-100 KeV) and relatively low atomic numbers (Z 20÷50) photoelectric effect dominates and it is possible to consider total linear attenuation coefficient only related to τ.

Due to the independence of X-ray interaction from physical and chemical state of the target, *photon mass attenuation coefficient* μ/ρ (cm^2/g) is usually used, whose values are tabulated in the NIST database [16].

$$I = I_0 e^{-\left(\frac{\mu}{\rho}\right)\rho x} \tag{1.3}$$

If a compound and not a single element is used as a target the total absorption depends on the absorption of different elements and on their relatives weights

$$\left(\frac{\mu}{\rho}\right)_{tot} = \omega_A \left(\frac{\mu}{\rho}\right)_A + \omega_B \left(\frac{\mu}{\rho}\right)_B + \omega_C \left(\frac{\mu}{\rho}\right)_C \tag{1.4}$$

where ω is the weight fraction of element in the compound.

The dependence of the attenuation coefficient from X-ray energy is presented in Fig.1.2 for Zinc and Cadmium, showing the decrease of the absorption coefficient for X-ray increasing energy and the K-edge discontinuity in correspondence of the photon interaction with the K-shell electron.

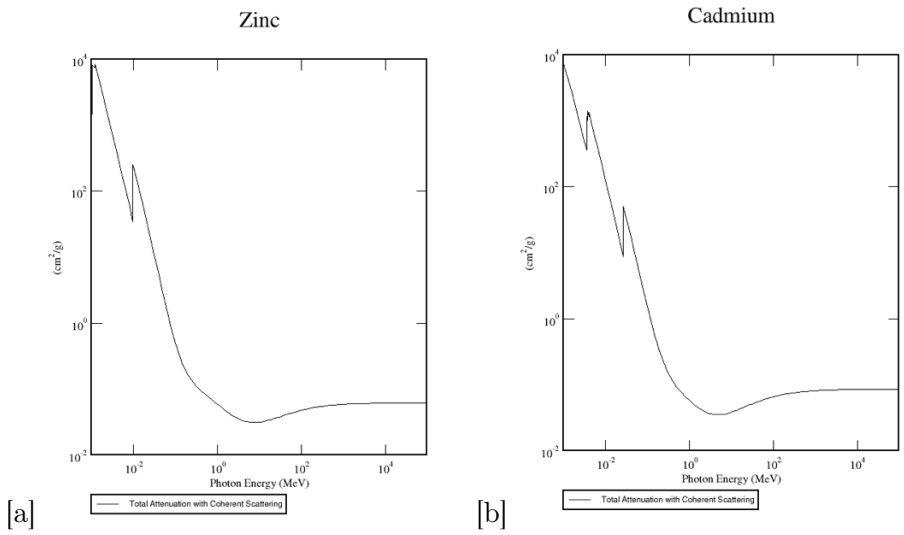

Figure 1.2: Zinc and Cadmium X-ray absorption coefficient

1.3 Quasi-monochromatic beams

We are investigating the K-edge technique using a portable device which consists of a quasi-monochromatic X-ray source, obtained via Bragg diffraction, of a standard X-ray beam on a mosaic crystal. This type of crystals are considered good candidates for monochromator design because of their high integrated reflectivity [14].
A defined beam energy can be set by choosing a suitable angle between source and crystal, in accordance to the Bragg law.
A mosaic crystal is formed by a large number of perfect microcrystallites which act like an aggregate of independently scattering ideal crystals with an angular distribution of the normal to the lattice planes that is roughly Gaussian [15]. As a consequence, the diffracted beam has a narrow energy band with an intrinsic energy spread related to the crystal spread ω and diffraction conditions. Diffraction conditions are determinate by using a incident nonparallel beams and this causes an additional energy and spatial spread. This type of crystal produces a quasi-monochromatic beam with a relatively high flux, necessary to perform imaging.

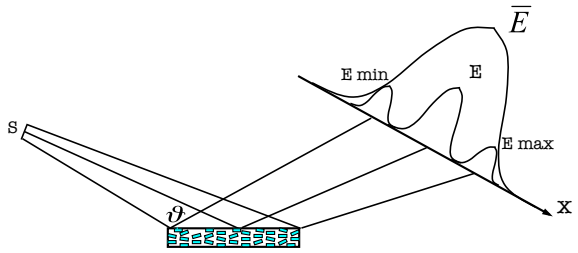

Figure 1.3: Bragg diffraction on a mosaic crystal with a nonparallel beam.

1.4 Image Processing

1.4.1 Image corrections

Digital images acquired, at lower and higher energy bracketing K-edge, must be submitted to a double correction for dark noise and beam inhomogeneity.

- *Dark field correction*
  Any signal resulting from solid-state detector present electronic noise generated by thermal motion of charge carriers and depends both from detector temperature and effective detection time.
  It's necessary to subtract from the radiographic image the *dark image*, acquired at the same condition of time exposition with no X-ray beam.

- *White field correction*
  Beams from X-ray tubes present spatial inhomogeneities that have to be corrected. To perform correction radiographic images are divided, pixel by pixel, by a *white field image*, acquired at the same condition of beam flux and energy, position and acquisition time with no target.

This two corrections allow to obtain a homogeneous and less noisy image.
Radiation damage of the detector causes increased surface dark current and detector response changes in linearity (view 3.3). In this case previous correction are no longer operating and is necessary to operate some software correction to obviate inhomogeneity.

1.4.2 Lehmann algorithm

To obtain a mass distribution (g/cm^2) of the investigated element on painting surface is necessary to process corrected image with Lehmann algorithm [4].
Lehmann algorithm produces two new images. The first one that gives the mass density distribution of the K-edge element $(\rho x)_{El}$. The second one gives the mass density distribution of all other materials in the sample $(\rho x)_{Other}$, expressed in terms of an overall low Z equivalent material [5, 6].

The signal in the raw images acquired is proportional to the number of photons impinging on the detector after transmission through the target

$$N(E_{\pm}) = N_0(E_{\pm})e^{\left\{-\sum_i \left[\frac{\mu}{\rho}(E_{\pm})\right]_i(\rho x)_i\right\}} \tag{1.5}$$

where N is the number of transmitted photons per unit of area, N_0 the number of incidents photons per unit of area, that correspond to *white field* image, E_+ and E_- energies of monochromatic beams (respectively higher and lower of K-edge), $(\mu/\rho)_i$ are the mass attenuation coefficients and $(\rho x)_i$ are the mass densities for thickness (in g/cm^2), and the subscript i denotes all different materials that compose the sample or painting (zinc, cadmium,oil, canvas, etc.).
For a beam with energy sufficiently close to the K-edge of the investigated element [17] we can assume that

$$(\frac{\triangle\mu}{\rho})_{El} \gg (\frac{\triangle\mu}{\rho})_{Other} \tag{1.6}$$

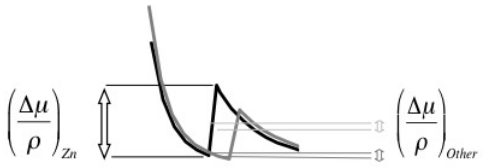

Figure 1.4:

Then it is possible to rewrite the sum on i in 1.6 as a sum of absorption of the analyzed element El, and the absorption of all the other elements expressed in terms of an overall low Z equivalent material. Choosing water as equivalent material:

$$\ln\frac{N}{N_0}(E\pm) = [\frac{\mu}{\rho}(E_{\pm})]_{El}(\rho x)_{El} + [\frac{\mu}{\rho}(E_{\pm})]_{H_2O}(\rho x)_{H_2O} \tag{1.7}$$

The mass attenuation coefficients (μ/ρ) at the two energies are known while the mass density (ρx) of investigated element and water are unknown quantities independent of beam energy. These latter quantities can be calculated, pixel by pixel, using

$$(\rho x)_{El} = \frac{[\frac{\mu}{\rho}(E_-)]_{H_2O}\ln\frac{N}{N_0}(E_+) - [\frac{\mu}{\rho}(E_+)]_{H_2O}\ln\frac{N}{N_0}(E_-)}{K_0} \tag{1.8}$$

$$(\rho x)_{H_20} = \frac{[\frac{\mu}{\rho}(E_+)]_{El}\ln\frac{N}{N_0}(E_-) - [\frac{\mu}{\rho}(E_-)]_{El}\ln\frac{N}{N_0}(E_+)}{K_0} \tag{1.9}$$

with

$$K_0 = [\frac{\mu}{\rho}(E_-)]_{H_2O}[\frac{\mu}{\rho}(E_+)]_{El} - [\frac{\mu}{\rho}(E_+)]_{H_2O}[\frac{\mu}{\rho}(E_-)]_{El} \tag{1.10}$$

By this way two final images are obtained: the first is the investigate element image, which is a map of the mass distribution of $(\rho x)_{El}$ and the other elements image, which is the map of all other materials expressed in terms of an equivalent material $(\rho x)_{H_2O}$.

1.5 Pigments

K-edge radiography allows to obtain the spatial distribution of one element in a painting layer.
If that element is peculiar of a pigment, the map of that pigment is obtained. In this section are shown elements with K-edge energy in the range 7-40 KeV and some pigments containing them.

Iron
Iron characterize some yellow-brown pigments, most of them derived from *Earths* and known since antiquity.
Siena Earth ($Fe_2O_3 \cdot nH_2O + Al_2O_3 + MnO_2$) is one of them. A compound of iron oxide, silicate clay and various impurities whose color derives from hydrate iron oxide and manganese dioxide. By heating is possible to obtain a darken pigment, *Burnt Sienna*.
When high manganese oxide percentage occur that turns the color to a hue green-brown and denomination of pigment change to *Umber* [11].
The presence of iron in all *Earths* does not allow to discriminate pigments with K-edge radiography alone.

Cobalt
Cobalt characterize antique pigments like *Smaltino*, known from Egyptian Age as glass, and artificial pigment like *Cobalt Blue, Cerulean Blue* and *Cobalt Green.*
Smaltino (potassic glass containing $CoO, SiO_2, K_2O, Al_2O_3$), is the most antique cobalt pigment. Is an artificial pigment since Egyptian Age and used as glass [11]. Only in Renaissance it began to be used like pigment, probably before XV century and widely used in XVII and XVIII centuries. From XIX was replaced by *Ultramarine Artificial Blue* and *Cobalt Blue*.
Cobalt Blue ($CoO \cdot Al_2O_3$), a deep blue with pure hue, is an artificial inorganic pigment invented at the end of '700 and obtained by combining cobalt oxide with aluminum salt by calcification [11].
Cerulean Blue ($CoO \cdot n(SnO_2)$) is another synthetic cobalt-containing pigment and, although introducts in 1821, it was not widely available until its reintroduction in 1860 in England [12].
Cobalt Green ($CoO \cdot ZnO$) is a mixture of cobalt oxide and zinc oxide discovered in 1780 but the poor tinting strength and high cost kept it in limited use [12].

Copper
Copper characterize some green pigments like *Verdigris, Scheele's Green* and *Malachite* and blue pigments like *Azurite* and *Egyptian Blue.*
Verdigris ($Cu(CH_3COO)_2 \cdot Cu(OH)_2$) is a synthetic pigment known by Egyptians, Greeks and Romans. Its has been made by corroding copper metal with acetic acid. Is an high transparent pigment used in tempera and oil paintings and miniated codes [11].
Scheele's Green ($2CuO \cdot As_2O_3 \cdot H_2O, 3CuO \cdot As_2O_3 \cdot 2H_2O, CuHAsO_3$ ..) is a synthetic pigment which was prepared first in 1775 by C. W. Scheele. Its variable composition depending on Cu and As fraction contained into initial material used. This pigment was rater unpopular due to toxicity derived from As [11].
The naturally occurring pigment *Malachite* ($CuCO_3 \cdot Cu(OH)_2$) is the oldest known green pigment. Mineral malachite occurs in egyptian tomb paintings and in european paintings; it seems to have been of importance mainly in the XV and XVI centuries [12].
A mineral usually associated in nature with malachite is *Azurite* ($2CuCO_3 \cdot Cu(OH)_2$), the most important blue pigment in European painting throughout the Middle Ages and Renaissance.
Occasional use began with Egyptians, it was uncommon until the Middle Ages when the manufacture of the ancient synthetic pigment *Egyptian blue* was forgotten [12].
Egyptian blue ($CaCuSi_4O_{10}$) is a copper calcium silicate, a very stable synthetic pigment. Is considered to be the first synthetic pigment and the most extensively pigments used from the early dynasties in Egypt until the end of the Roman period in Europe [12].

Zinc
Pigments containing zinc are white pigments like *Zinc White* and *Lithopone* and other color pigments like *Cobalt Green* and *Yellow Cadmium.*
Zinc White (ZnO) is a synthetic pigment known from 1782 and trade in the second half of the XIX century [11].
Lithopone ($ZnS + BaSO_4$) is a synthetic pigment invented at the end of XIX century by Guillame Ferdinand and used in place of Lead White; it has a greater hiding power than Zinc White [11] .
Yellow Cadmium (CdS), as will be discussed later, is synthetic pigment that does not contain zinc but in natural form exist a cadmium sulphide that contains zinc sulphide also ($CdS + ZnO$) [11].

Arsenic
Arsenic is contained in pigments like *Orpiment, Realgar* and, like mentioned above, in *Scheel's Green.*
Orpiment (As_2S_3) is natural pigment, which naturally occurred widely but in relatively small deposit.
It was known to Egyptian, Greeks and Romans and used from XII to XVII but abandoned in XIX for its toxicity. It was used to simulate gilding and during Middle Age was used in miniated codes [11].

Realgar (As_4S_4) is a red orange natural pigment closely related to the yellow orpiment. The two minerals are often found in the same deposits. Although it occurs perhaps as widely in nature as orpiment, realgar appears not to have been used so widely. Realgar is an highly toxic arsenic sulfide and was the only pure orange pigment until modern *Chrome Orange* [12].

Strontium
Strontium yellow ($SrCrO_4$) is a synthetic inorganic pigment created in the XIX century. Is light-sensitive and can form green chromium oxide [11].

Molybdenum
Molybdenum Orange ($PbCrO_4 \cdot PbSO_4 \cdot PbMoO_4$) is a synthetic inorganic pigment described in 1863 and traded in the next century [11].

Cadmium
The range of cadmium pigments, yellow, orange and red are basically *Cadmium Yellow* (CdS) with some selenium added in place of sulfur ($CdSe$).
Indeed, mineral pigment produced from cadmium sulphide when heated with selenium becomes red.
Cadmium red was available as a commercial product from 1919 but used sparingly due to the scarcity of cadmium metal and therefore because it was more expansive [12].

Tin
Tin is contained in *Tin White, Lead-Tin Yellow* and *Cerulean Blue*, previously shown in 1.5.
Tin white (SnO_2) is synthetic pigment, used in Europe from XVI to XVII centuries into miniated code [11].
Also *Lead-Tin Yellow* ($PbSnO_4$; $Pb(Sn, Si)O_3$) is synthetic pigment, discovered in the XIII century, and used until XVIII but most common from XV and XVII centuries.
There are two different pigments type: I and II. First is lead tin oxide and most frequently found on old paintings. Type II may contain free tin oxide and additional silicon [12].

Barium
Two white pigments contains Barium, aforementioned *Lithopone* and *Bianco Fisso*. The second one ($BaSO_4$) is a transparent white pigment, used mixed with other pigments or as glaze [11].

Chapter 2

Experimental apparatus

The K-edge radiography facility installed at Larix Laboratory, at Department of Physics in Ferrara, are developed from a previous prototype, by Gambaccini et al [8], for K-edge mammography. For this work, a new prototype system has been developed to provide K-edge radiography on samples and painting.
The imaging system, presented in figure 2.1 provides via Bragg diffraction a tuneable narrow energy band X-ray in the 7-40 KeV range using a mammographyc X-ray tube.

2.1 X-Ray tube

X-ray source used is a mammographic X-ray tube, XM 12 manufactured by I.A.E [1] with rotating Molybdenum anode, 0.5 mm Beryllium window and a nominal focal spot size 0.3 mm^2. The X-ray tube is powered by a high-frequency, high-voltage generator Compact Mammo-HF [2].
The source has been chosen to obtain high flux by an anodic current, which can rise up to 100 mA, depending on the set-up conditions, associated to relatively low voltages, from 16 KV onwards to a maximum of 41 KV. High flux is required to obtain high signal and low KVp is necessary to select, via Bragg diffraction, only the first order diffraction at the desired energy.
The system monitors KVp values with an uncertainty of $\pm$ 0.1 KV and the anodic current with an uncertainty of $\pm$0.05 mA.
The X-ray power supply allows a choice between two conditions of work:

- Low current (Scopia)
  This setting allows long exposition time, up to 300 second, and current supply is limited to low values, lower than 15 mA. Scopia setting is generally used for beam analysis, where long exposition are recommended for good statistics and low flux avoid saturation of the detector.

[1] I.A.E. Spa, Milano, Italy
[2] Metaltronica Srl, Roma, Italy

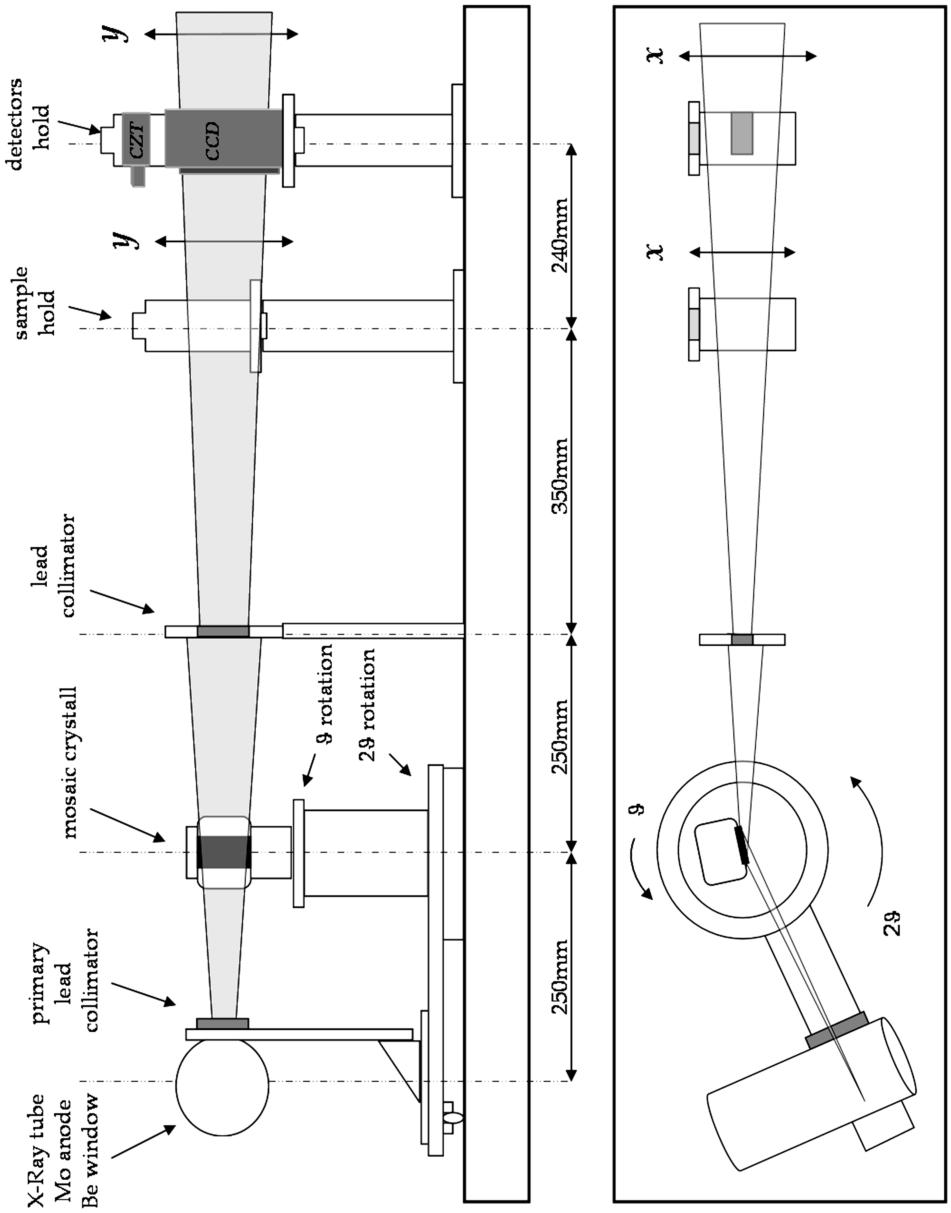

Figure 2.1: K-edge facility.

- High current (grafia)
  Allows short exposition time, 5 seconds maximum, but current higher than 50 mA. High current is needed for imaging, especially with K-edge analysis of painting where flux of monochromatic beam is low.

Is possible to choose between different current position, from 1 to 6, but an effective monitoring of current value is provided by power supply monitor. Some typical KVp and anodic current used for imaging and spectral measurement are reported in table 2.1.

Element	K-edge Energy (KeV)	KVp (KV)	Anodic Current (mA) *"Scopia"*	*"Grafia"*
Fe	7.11	16	4.30	56.5
Co	7.71	16	4.30	56.5
Cu	8.98	18	4.40	56.5
Zn	9.66	18	4.30	73.1
As	11.87	23	11.15	113.0
Cd	26.71	41	2.15	86.1
Sn	29.20	41	2.15	82.5

Table 2.1: Some typical working condition for spectrum and imaging analysis

2.2 Mosaic crystal

The bremsstrahlung beam is monochromatized by a highly oriented pyrolytic graphite mosaic crystal (HOPG)[3], $60\times28mm^2$ wide and $1mm$ thick with nominal a mosaic spread of 0.28°.

2.3 Optical bench

The imaging system is presented in Fig.2.1.
The X-ray tube is mounted on an arm fixed to a motorized goniometer Microcontrole[4] rotating with an accuracy of 0.001° from 0° to a maximum angle of 2θ=90°.
The mosaic crystal is placed 250 mm away from the X-ray focal spot on a motorized tilt/linear stage in order to enable optimal alignment of the apparatus. The system is mounted on another isocentric goniometer that can rotate with an accuracy of 0.001° to a maximum angle of θ=45°.
This set-up provides a monochromatic beam always perpendicular to the imaging plane independently of the tuned X-ray energy. The monochromatic beam, at a 250 mm distance from the crystal is collimated by a 8 mm wide lead slit.
A motorized scanning system is placed 350 mm downstream the first collimator and is used as a support for the painting, which can be scanned by this automated system. A second motorized scanning system is placed 240 mm away from the first (1090 mm distance from the X-ray focal spot) and is the support for the detectors. All the scanning systems and goniometers are connected to a multi axis motion controller unit [5].

[3]Optigraph Ltd, Moscow, Russia
[4]Microcontrole, Evry, France; now Newport, USA
[5]Motion Controller MM 4006, Newport Corporation, CA, USA

2.4 Detectors

Three different detectors have been used to perform spectrum analysis and K-edge elemental mapping.

- **Spectrum analysis**
  To perform spectral analysis a cadmium zinc telluride detector (CZT) was used. XR-100T-CZT [6] is a solid-state detector with $25mm^2$ area, 2 mm thickness, 250 μm beryllium window and a resolution of 900 eV FWHM at 59 KeV .
  Within the energy range considered in this work, 7-40 KeV, the efficiency of the CZT detector is approximately 100% [18].
  In order to reduce the X-ray photon fluxes on the detector a pinhole with a diameter of 224 μm has been used.

- **Imaging**
  Two silicon detectors have been used to perform a comparison of element recognition of different imaging detectors: a commercial Charged Coupled Device, CCD S7199 [7], and a Silicon Strip Detector (SSD) realized by FBK [8] on a design by the Department of Science and Advanced Technology of Piemonte Orientale University.

  - **CCD**
    The Hamamatsu CCD is a FFT (Front-Illuminated) detector without FOS (Fiber Optic plate with Scintillator).
    The CCD has a nominal thickness of 300 μm, a total active area of 3072×128 pixels (two different CCD chips, 1536×128 pixels) and 48μm pixel size which allows a good spatial resolution.
    The first layer of FOS, the scintillator, converts high energy photons to visible light and fiber optics allow a high efficient photon transport to the CCD surface. This type of structure prevents radiation damage on Silicon surface by stopping high energy photons reaching the bulk.
    However the FOS layer presents two significant defects: on one hand resolution get worst due to non direct detection on the Silicon surface. On other hand low energy X-ray photons are converted on the first layer of scintillator surface so visible photons don't reach the Silicon active area, making the efficiency lower. To improve efficiency at low energy and spatial resolution a CCD without FOS has been chosen.
    This choose, like illustrate in chapter 3, has let to a radiation damage.
    CCD electronics allows to set gain and offset for the two detectors independently to obtain an homogeneous signal [19].

[6] Amptek inc., MA, USA
[7] Hamamatsu Photonics K.K., Japan
[8] Fondazione Bruno Kessler, Trento, Italy

– **SSD**
The SSD has been realized with 512 Si-strip, 1 cm thick and 300×100 μm pixel size. It is a Edge-on detector and it works in single photon counting mode [20]. Edge-on configuration allows a major penetration thickness to increase efficiency in the 20-40 KeV energy range. To ensure a very small dead area of the SSD working in this configuration, the detector is cut perpendicular to the strips at a distance of only 20 μm from the end of the strips.
The SSD electronics allows to perform a calibration for each single strip to obtain a homogeneous response along 512 strips. It is also possible to set two different energy thresholds to acquire independent signals at two different energies.

Chapter 3

Radiation damage on CCDs

In solid state detector high radiation dose may cause radiation damage. Different types of effects can occur: defect on charge transfer, high dark current, ghost images are often observe.
In the following section CCD structure, working principle and radiation damage will be discussed.

3.1 Charge Coupled Device

Usually this types of detectors are used as imaging detectors, integrating all interacting photons. Depending on the read-out electronics, counting mode is also possible.
When photons interacts with semiconductor layer electron-hole pairs are generated proportionally to the energy of the incident photons. The generated charge is stored in each pixel and sequentially transferred from adjacent pixels and read-out at the end of the pixel line, as illustrated in next section.

3.1.1 Structure

Figure 3.1, from [21], show the section of a Front Illuminated, Two-Phase CCD, based upon a MOS (Metal Oxide Semiconductor) capacitor.
Front illuminated CCD (FI-CCD) identify detectors that receive and detect light form the front side, where electrodes are positioned.
Two phase signals are applied to two metal electrodes (P1, P2) for each pixel used to transfer charge.
Fig.3.1[a] shown a two phase CCD structure, based on non-conductive oxide layer, a Silicon Dioxide layer SiO_2 and semiconductor channel of Si is present as base layer.
When a voltage is applied to the *gates* (P1 and P2) a *depletion zone*, with a thickness of few microns, is created.
Thanks to the potential applied during the integration period charge generated by photons interaction is stored in the potential well region in the photosensitive section.

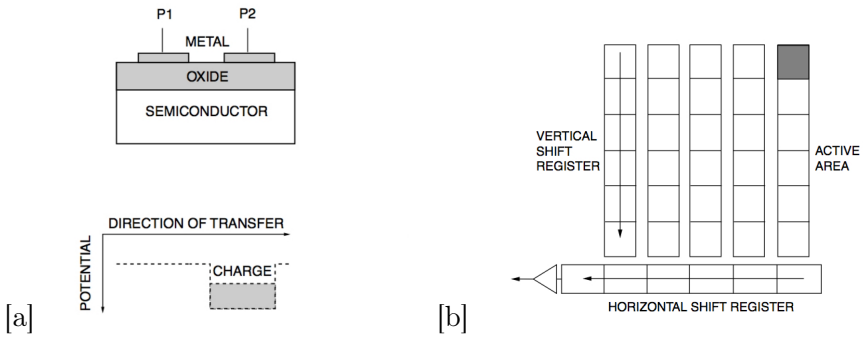

Figure 3.1: CCD structure, from [21]

By applying two clock pulses with different voltage levels to the electrodes charge is sequentially transferred from pixel to pixel.
Read-out is controlled by the CCD register, composed of three different sections, as shown in Fig.3.1[b].
The *Vertical register* are the photosensitive pixels, grouped in columns (in our detector 128), which carried out collected charge at the end of the columns. The *Horizontal register* collect this signals and transfer charges to Chip amplifier. The *Chip amplifier* convert the charge derived from Horizontal register to a voltage signal.

3.2 Optimization of the system

For CCD imagers there are three major sources of *dark current*, i.e charge generation with no incident light.

- Thermal generation and diffusion in neutral bulk region
- Thermal generation in depletion zone
- Thermal generation due to surface state at $Si - SiO_2$ interface

Of these sources, the contribution from interface states is the dominant contributor of dark current for multi-phase CCDs [21].
Since either case is associated with heat or temperature, the dark current has a strong correlation with temperature.
To obtain a good signal-to-noise ratio is necessary to minimize dark current. Two methods are presented in the following to achieve that aim: cooling and optimization of the gate's voltage.

3.2.1 Cooling

As mentioned above dark current is correlated with device temperature. For CCD used it doubles for every 5 to 7°C increase in temperature [21]. A cooling system is usually realized with a Peltier cell under or behind detector.

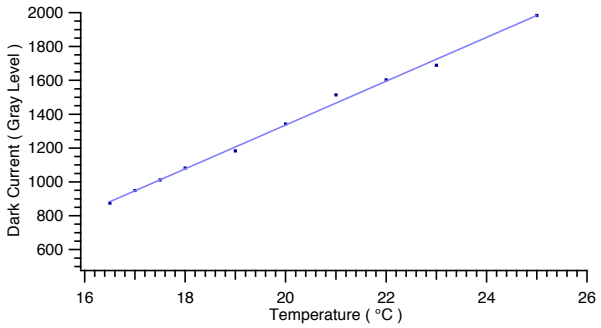

Figure 3.2: Measured dark current as average gray level vs. detector temperature

Our detection system present a double Peltier cell under CCD, one for every part of the detector.
A cooling test has been realized acquiring dark images at different temperatures.
As illustrated in figure 3.2 the dark current, evaluated by average gray levels in the CCD image, is decreasing as temperature decreases.
Unfortunately at present our custom electronics does not support a permanent cooling system: it is not sealed and humidity deposition on electronics is unavoidable. This cooling system has not been used.

3.2.2 Optimization of the gate voltage

As mentioned above the contribution from interface states (from Si and SiO_2) is the dominant contributor of dark current for multi-phase CCDs.
Dark current generation at this interface depends on two factors, namely the density of interface states and the density of free carriers (holes and electrons) that populate the interface [22].
Electrons that thermally "hop" from the valence band to an interface state (sometimes referred to as a mid-band state) and to the conduction band produce a dark e-h pair. The presence of free carriers will fill interface states and, if the states are completely populated, will suppress hopping and conduction and substantially reduce dark current to the bulk dark level.
In MPP technology, Multi Pinned Phase, also referred as *inverted operation*, dark current is significantly curtailed by inverting the signal carrying channel by populating the Si-SiO_2 interface with holes which, as mentioned above, suppresses the hopping conduction process [22].
For pinning to occur, the gate voltage is made increasingly more negative. At certain negative gate voltage the valence band at the Si-SiO_2 interface reaches the potential of the valence band in the bulk semiconductor.
If substrate is grounded, the holes from that channel stop region "pin" the valence band to ground and no additional charge in channel potential occur. The voltage at which this occur is called the *pinning gate voltage*.
This is implemented by setting all MOS gate to the inverted state [21].
In a two phase CCD, like our instrument, a potential difference is present by means of

ion implantation between the collecting and the barrier phase.
This means the CCD still provides the potential well even when all the gate are set to the same voltage. MPP operation is then performed applying a bias so all phases of the CCD are set to the inverted state.
This inversion cause the conduction proprieties of the semiconductor to change from P-type semiconductor to N-type or vice-versa.
As shown in the potential distribution in figure 3.3, from [21], both the collecting and barrier phase are pinned in the inverted state. In the pinning state the CCD surface is inverted by holes supplied from the channel stop region. The potential at Si-SiO_2 interface is pinned and fixed at the same potential as the substrate, even if a further negative voltage is applied [21].

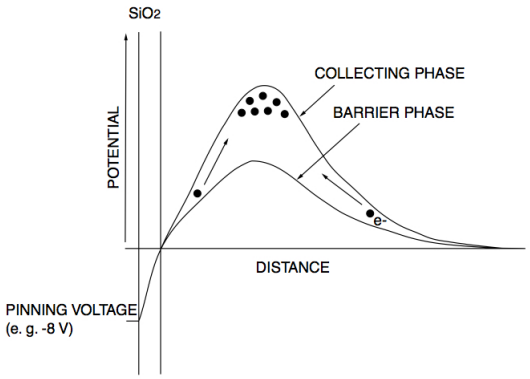

Figure 3.3: Potential schematization in MPP, from [21]

In this state while inverted by hole, thermally generated electrons at Si-SiO_2 interface can be dramatically suppressed, thus achieving a very low dark current.
In MPP operation is important to apply an optimum pinning voltage since the greatly affects the dark current characteristics. As illustrated in figure 3.4[a], from [21], the dark output cannot be reduced to a minimum level because the inverted layer is not fully formed by holes.

To optimize our system a study of optimum pinning voltage has been achieved.
Our custom electronics allows to control the two gate voltage separately and so interact directly with voltage setting.
Has been measured dark current with 2 seconds of exposition time without X-ray and changing gates voltage. As shown in figure 3.4[b] dark current has been decreased setting gate voltage below -8 V.

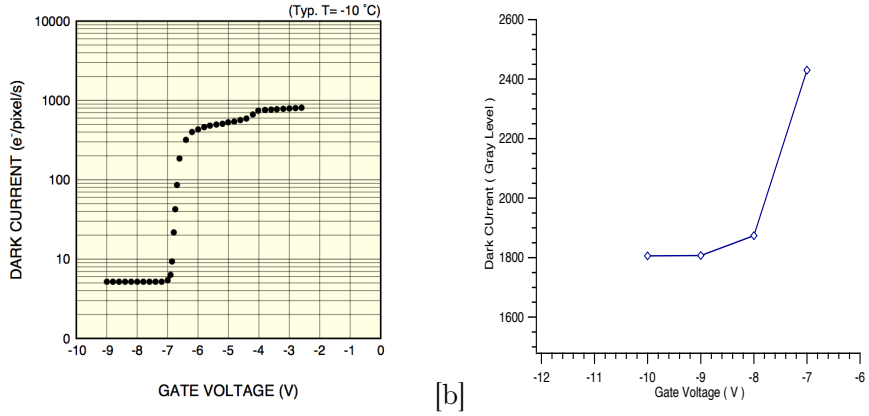

Figure 3.4: Decrease of dark current decreasing gate voltage: [a] from [21] and [b] result obtained on CCD S7199.

3.3 Radiation Damage

Radiation effects on CCD detector can be various and two major classes can be identified.
First are cumulative effects derive from total ionizing dose (TID) and displace damage and second classified as single event effects (SEE).
Working with low energetic photons while cumulative effect derived from TID can occur, displace damage or single event effects cannot.
In general TDI damage interest the oxide and the bulk-oxide interface through ionization. This form of damage results in changes in the flat band voltage, increased surface dark current and changes in linearity.

- **Flat Band Shift**
  Ionization-induced damage induces a build-up of charge in the CCD's gate insulator causing a change in the flat band voltage namely *flat-band shift*.
  Analyzing our CCD detector a change in the flat band voltage has been found out and, working as explain above, effect of increased surface dark current derived from shift in the flat band voltage has been alleviated by re-setting a new optimized gate voltage (view 3.4 [b]).

- **Dark current**
  In addition electrons traps has been created by radiation damage at the silicon-silicon dioxide interface which slowly de-trap into the pixel's potential well causing the CCD's dark current to increase.
  Figures 3.5 and 3.6 shown radiation damage suffered by CCD detector after 2 working year and approximately a total flux of $6{\cdot}10^9$ photons/mm^2 in energy range 9 - 10keV .
  Images in Fig.3.5 are acquired with the same time exposition, reported in a 8-bit grayscale and shown with the same contrast and luminosity to obtain a correct results interpretation. Fig. 3.5[a] is the image obtained with a new CCD, never

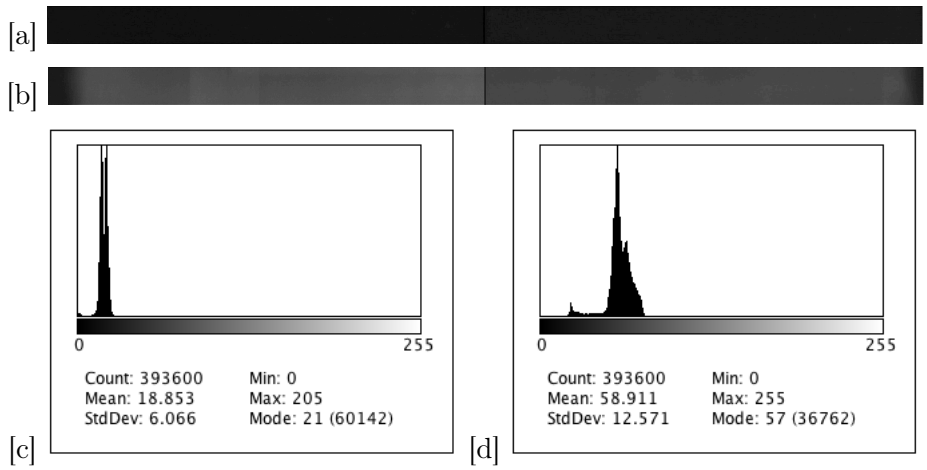

Figure 3.5: Comparison between images and histograms of the new CCD [a,c] and the CCD with radiation damage [b,d] with same exposition time.

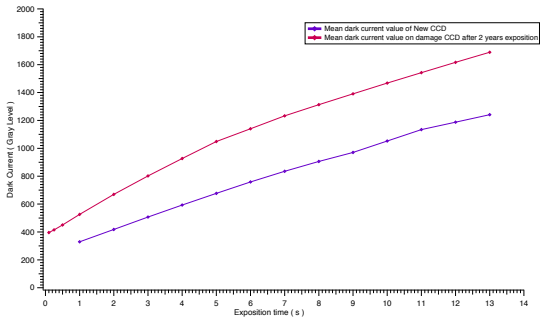

Figure 3.6: Plot of increasing of dark current effect after radiation damage

exposed to X-rays, and 3.5[b] the same CCD after two working years with X-rays. Histograms of the images are presented in Fig. 3.5[c,d].
Analyzing this comparison dark current increase is evident on all CCD surface and some residual images are visible. This is due to a non homogeneous dose suffered by detector and consequently a non-homogeneous radiation damage.
Plot in Fig. 3.6 represent mean gray level value on all CCD surface for different time exposition, for the CCDs new and damaged.

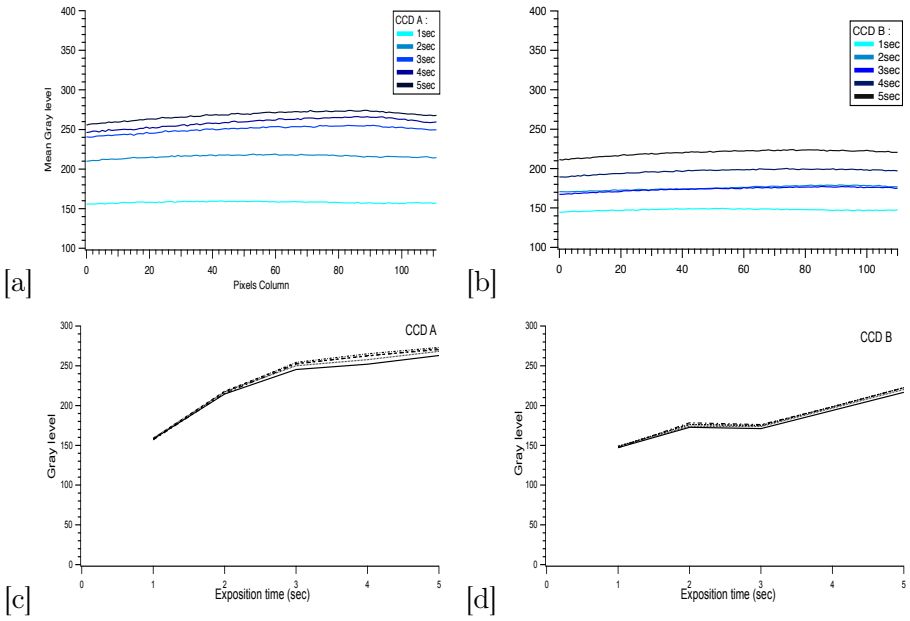

Figure 3.7: Changes in linearity with radiation damage

- **Changes in linearity**
  Images at same energy, 10 KeV, same anode current and increasing exposition time, from 1 to 5 seconds, have been taken. In Fig. 3.7[a,b] the plot of mean column values, shown separated for the two different part of detector, namely CCD A and CCD B, is shown. The same result, as mean gray levels obtain vs. exposition time, is shown in Fig. 3.7[c,d].
  As expected different behavior of the two detectors is highlighted and a not linear response to X-ray intensity increased is shown. In this working condition a *white field correction* and Lehmann algorithm does not work correctly.

Chapter 4

Characterization of the X-ray source

With our facility 7-40 KeV energy range has been investigated where K-edge of more elements that characterize pigments are located, as illustrated 1.5.

4.1 Measurement setting

CZT detector has been used to perform spectrum analysis of the source in different KVp and energy conditions.
All measurement have been performed positioning detector on the last motorized system at 1090 cm from the focus of the tube.
Deriving from the many degrees of freedom of the system a not perfect alignment from goniometers and crystal entails a slight deviation of the center of monochromatic beams from the geometrical center on imaging plane.
It has been taken into account finding the center of monochromatic beams identified as the maximum signal position.
A small lead collimator, with $224 \pm 13 \mu m$ diameter, has been used in front of CZT detector.
Further, an analysis was performed to determine detector energy resolution in our energy range. The nominal energy resolution is explicitly indicated by datasheet only for 59.5 KeV Am^{241} peak energy.
Beam energy has been set at K-edge energy of Iron, Cobalt, Copper, Zinc, Arsenic, Bromine, Strontium, Molybdenum, Silver, Cadmium, Tin and Barium.
In order to characterize quasi-monochromatic spectra, an analysis has been realized at the K-edge beam energies; also slightly lower energy (E_-) and slightly higher energy (E_+) have been analyzed.
The choice of energy "low" and "high" was done as a compromise between the two competing requirements of having lower energy difference from Low and High energy beams and of the minimum superposition of the spectra. For energy beams from up to Bromine K-edge (13.47 KeV) an energy distance of 1.3 KeV between high and low beams was chosen.

At higher energy more spacing was necessary due to the spread of monochromatized beams.
Bremsstrahlung spectrum of the source has been analyzed at the same KVp condition of monochromatic beams to calculate monochromatization efficiency of the crystal.
Integrated reflectivity has been calculated by compared photon flux of continuous and monochromatized beam in the same energy range, related to crystal spread.
Let θ the Bragg angle and ω the mosaic spread of the crystal, diffracted beam has a narrow energy band related the angle range
$\theta + \omega < \theta < \theta - \omega$.
Photons in this energy range, $E_{\theta-\omega} < E_\theta < E_{\theta+\omega}$, have been considered for monochromatization efficiency.
All results are presented in term of normalized total flux, $photon/mAs \cdot mm^2$.

4.2 CZT energy resolution

In order to perform a complete characterization of the system, a preliminary measurement has been done to measure effective energy resolution of the CZT detector.
Two reference sources, Am^{241} and Co^{57}, have been analyzed.
Resulting peak widths have been calculated and the energy resolution found is shown in Fig 4.1.

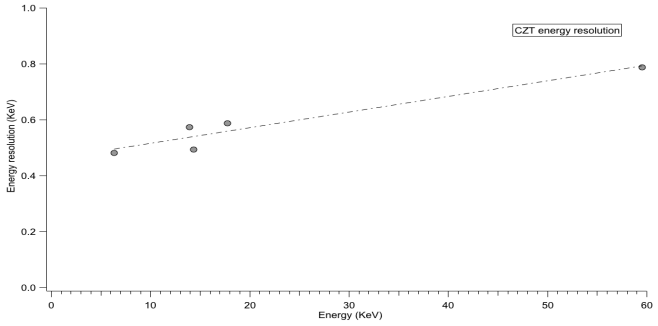

Figure 4.1: CZT energy resolution measured

4.3 Iron K-edge: 7.11 KeV

To realize analysis at Iron K-edge energy would be necessary to set KVp to prevent the second order diffraction. Unfortunately our system does not allows to set a KVp lower than 16KV and second harmonic has been generated.
In Fig 4.2 a comparison between continuos beam and monochromatic beam at Iron K-edge energy (7.11 KeV), both setting KVp at 16KV, is show.
Fig.4.3 shown quasi-monochromatic spectra obtained at slightly lower energy (E_- 6.46 KeV) and slightly higher energy (E_+ 7.76 KeV).
As explain above, set of KVp has generated second order diffraction beam. Its has been product only for the lower energy beam and its peaked on 13KeV.
However, by using a SSD this can be eliminated by threshold setting. With our traditional CCD this energy configuration to investigate Iron cannot be used.
Monochromatization efficiency has been calculated by compared photon flux of continuous and monochromatized beam in the energy range related to crystal spread. Only first diffraction order has been take in account. Only a small fraction of the beam (15.2%) has been monochromatized.
In Fig 4.4 are present monochromatic spectrum with only first diffraction order and residuals relative to the gaussian fit.
Table 4.13 show energy beam set, peak position, energy resolution and total photon flux of the beam.
Setting diffraction angle to obtain Fe K-edge energy, 7.11 KeV, energy peak of 7.18 KeV is obtained.
This slight deviation depends on the mechanical misalignment.

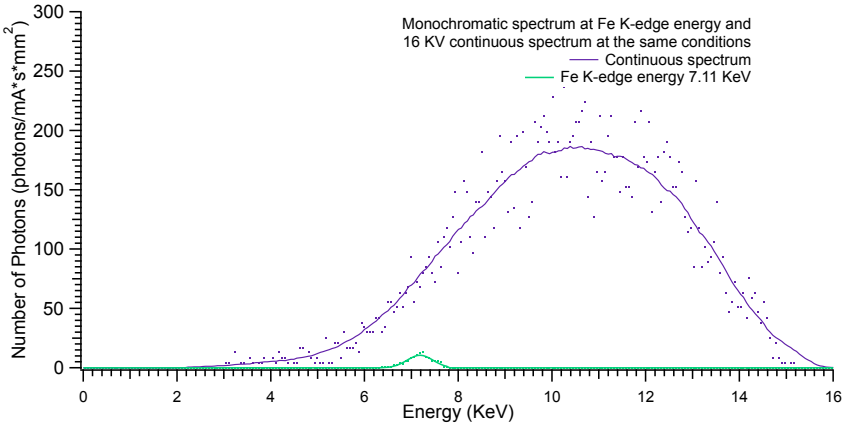

Figure 4.2: Fe: Bremsstrahlung spectrum at 16 KVp and monochromatic beam on K-edge energy

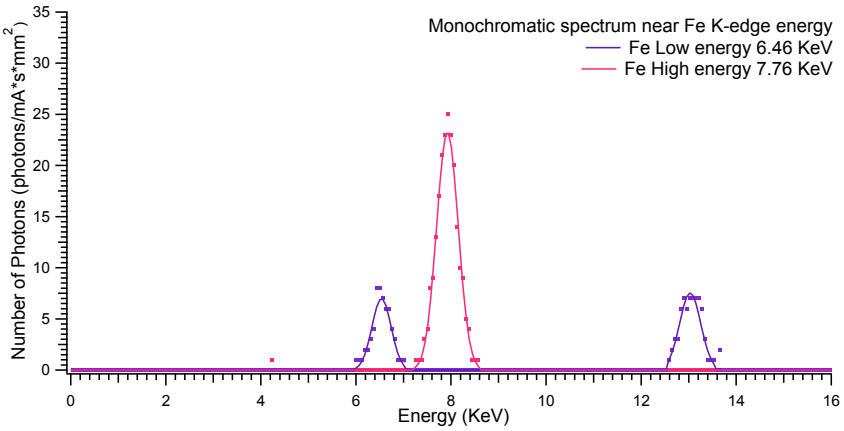

Figure 4.3: Fe: First and second order diffraction of Fe

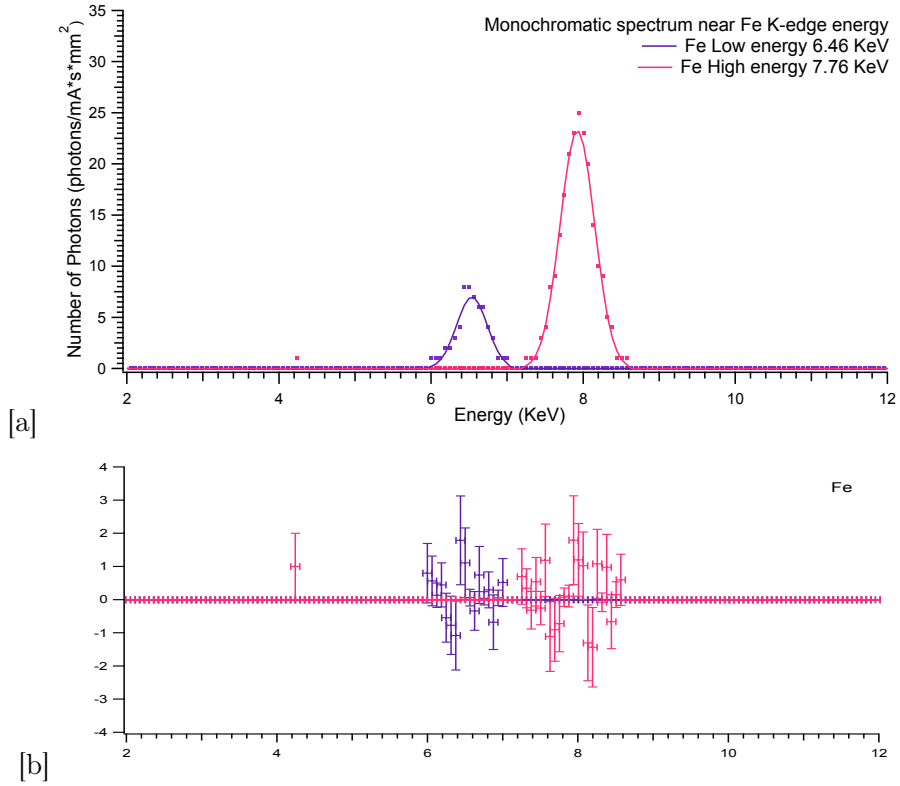

Figure 4.4: Fe: [a] monochromatic beam on energies bracketing K-edge energy and [b] residuals relative to the gaussian fit

Fe	Setting Energy KeV	x_0 KeV	FWHM KeV	Flux $ph/mm^2 * mA * s$
K-edge	7.11	7.18	0.47	115 ±11
Low	6.46	6.54	0.34	56 ±7
High	7.76	7.92	0.38	211 ±15

Table 4.1: Characteristics of the diffracted beams on Iron K-edge energy.

4.4 Cobalt K-edge: 7.71 KeV

At Cobalt K-edge energy the same KVp of Iron measures has been set.
Fig. 4.5 show a comparison between continuos and monochromatic beam at Cobalt K-edge energy, both setting KVp at 16KV.
A slightly increased energy photon flux at this higher energy is found: $212 \pm 15 ph/mm^2 \cdot mA \cdot s$ at K-edge energy and a monochromatization efficiency of 17.7% is found.
In Fig. 4.6 are present monochromatic spectrum and residuals relative to gaussian fit; table 4.2 show spectra data obtained.

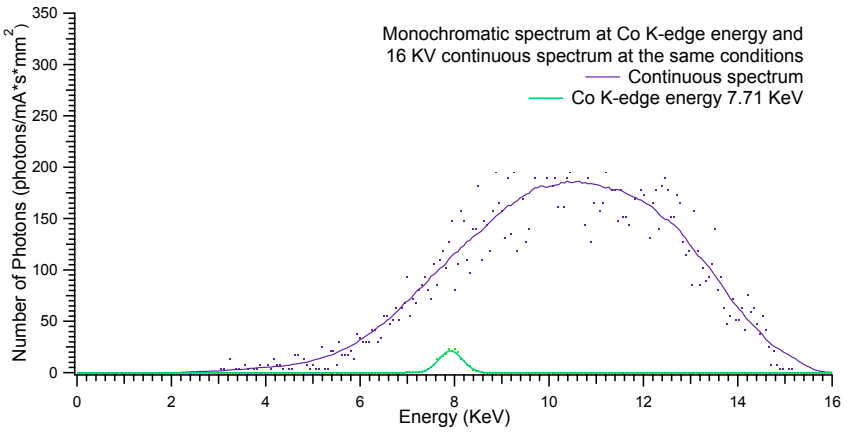

Figure 4.5: Co: Bremsstrahlung spectrum at 16 KVp and monochromatic beam on K-edge energy

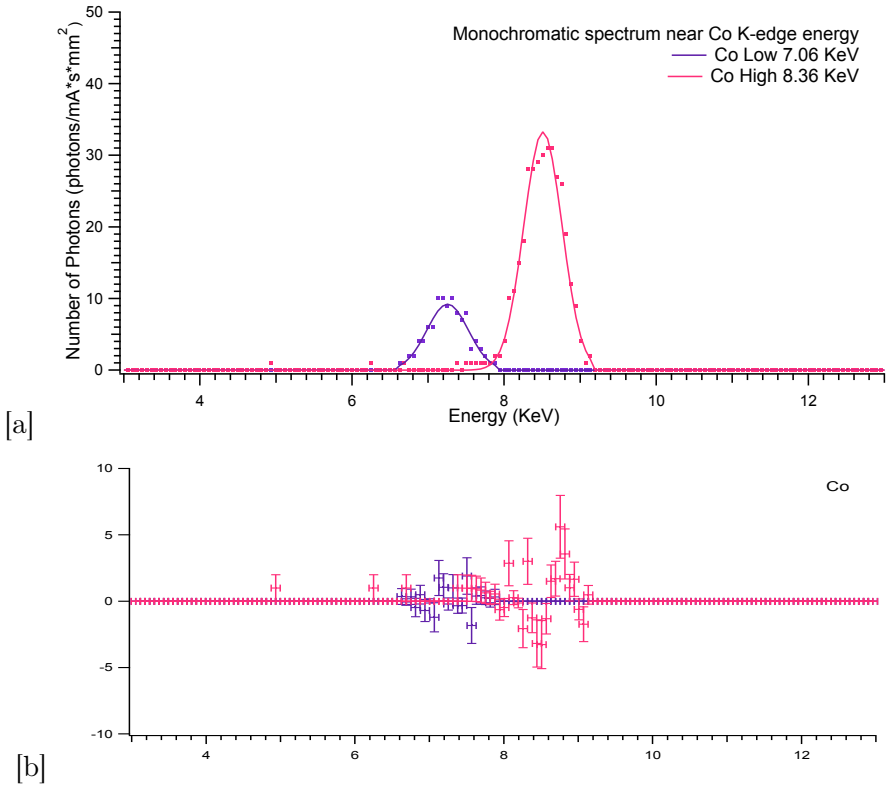

Figure 4.6: Co: [a] monochromatic beam on energies bracketing K-edge energy and [b] residuals relative to the gaussian fit

Co	**Setting Energy** KeV	x_0 KeV	**FWHM** KeV	**Flux** $ph/mm^2 * mA * s$
K-edge	7.71	7.91	0.42	212 ±15
Low	7.06	7.26	0.46	99 ±10
High	8.36	8.51	0.46	333 ±18

Table 4.2: Characteristics of the diffracted beams on Cobalt K-edge energy.

4.5 Copper K-edge: 8.98 KeV

For the Copper K-edge spectrum an increased value of KVp at 18 KV has been used.
As shown in Fig. 4.8 and reported in table 4.3 a KVp increasing correspond to a photon flux increase and at 9.17 KeV flux of $600 \pm 24 ph/mm^2 \cdot mA \cdot s$ is obtained. In this case a monochromatization efficiency of 22.3% is found.

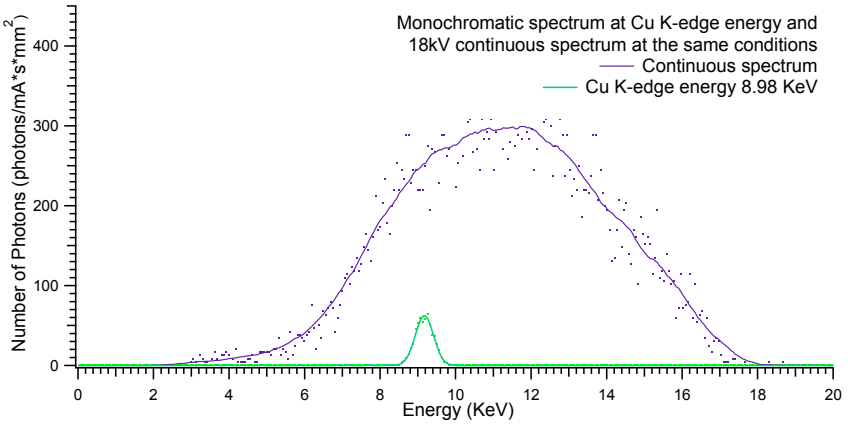

Figure 4.7: Cu: Bremsstrahlung spectrum at 18 KVp and monochromatic beam on K-edge energy

Cu	**Setting Energy** KeV	x_0 KeV	**FWHM** KeV	**Flux** $ph/mm^2 * mA * s$
K-edge	8.98	9.17	0.40	600 ±24
Low	8.33	8.48	0.33	497 ±22
High	9.63	9.82	0.40	781 ±28

Table 4.3: Characteristics of the diffracted beams on Copper K-edge energy.

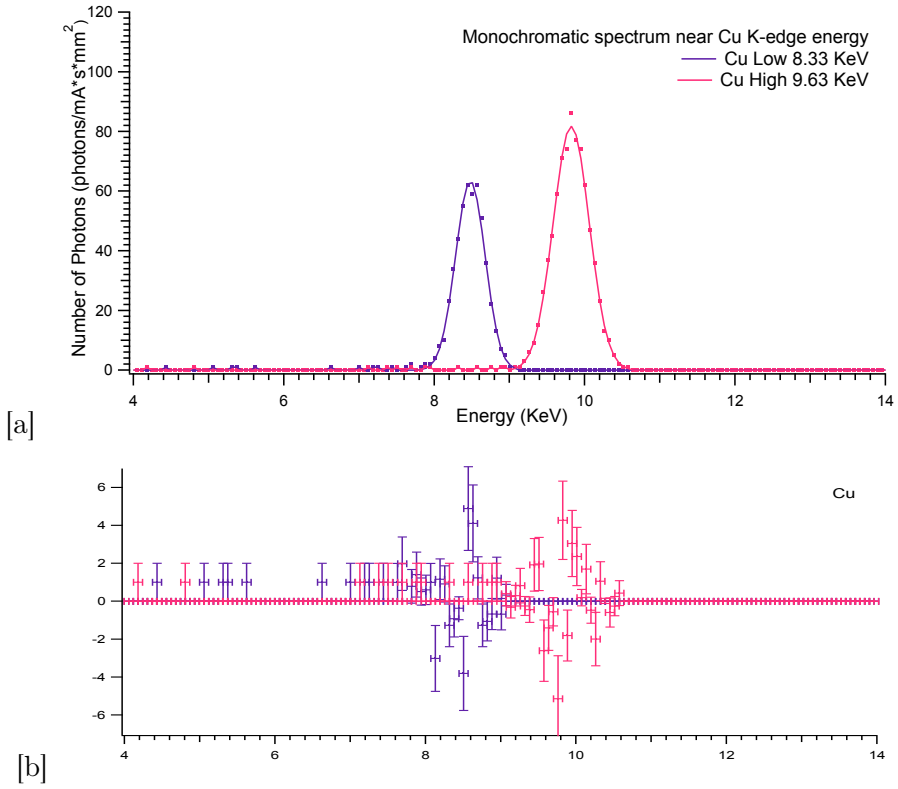

Figure 4.8: Cu: [a] monochromatic beam on energies bracketing K-edge energy and [b] residuals relative to the gaussian fit

4.6 Zinc K-edge: 9.66 KeV

To perform spectrum analysis at Zinc energies is used a KVp of 20 KV and a monochromatization efficiency of 30.7% is obtained.
As shown in Fig. 4.10 and reported in table 4.4 increasing energy beams increase slightly deviation of the energy beams, in this case about 0.2 KeV; beams energy of 9.87 KeV, 9.26 KeV and 10.52 KeV are obtained.
Photon fluxes of 940±31, 708±27 and 1098±33 $ph/mm^2 \cdot mA \cdot s$ are obtained.

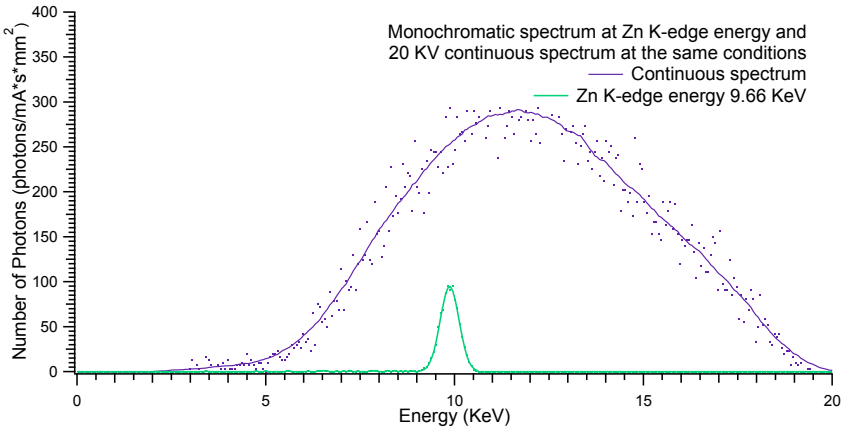

Figure 4.9: Zn: Bremsstrahlung spectrum at 20 KVp and monochromatic beam on K-edge energy

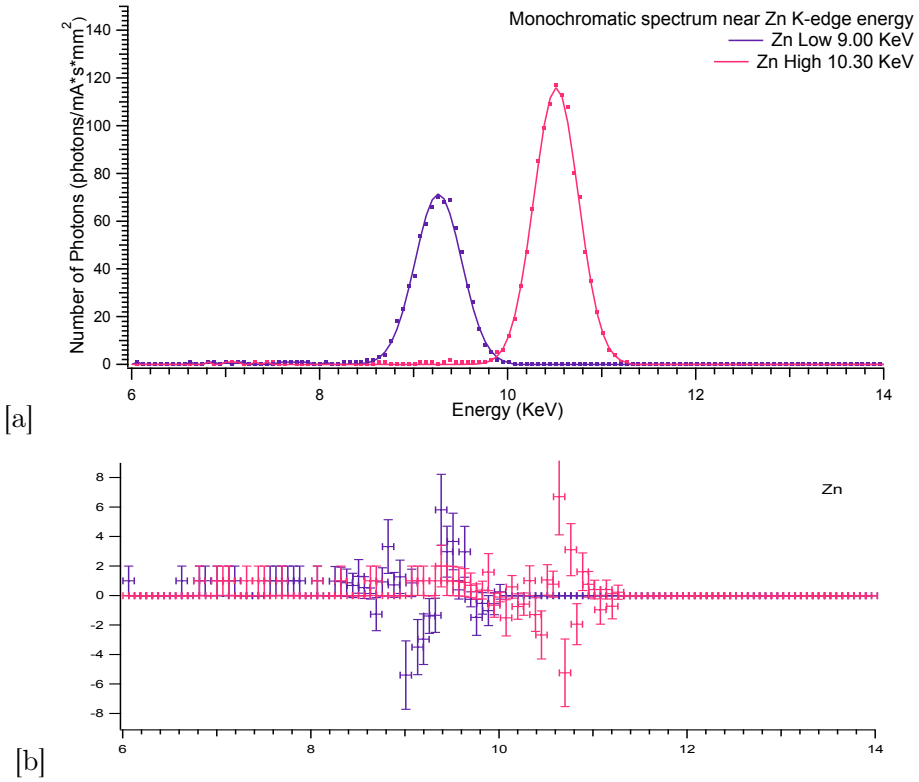

Figure 4.10: Zn: [a] monochromatic beam on energies bracketing K-edge energy and [b] residuals relative to the gaussian fit

Zn	**Setting Energy** KeV	x_0 KeV	**FWHM** KeV	**Flux** $ph/mm^2 * mA * s$
K-edge	9.66	9.87	0.42	940 ±31
Low	9.00	9.26	0.42	708 ±27
High	10.30	10.52	0.40	1098 ±33

Table 4.4: Characteristics of the diffracted beams on Zinc K-edge energy.

4.7 Arsenic K-edge: 11.87 KeV

To perform measure at Arsenic energy has been used 23 KV.
In Fig.4.11 are shown Bremsstrahlung spectrum of the source and monochromatic spectrum at As K-edge energy. At this KVp emission peaks of the Molybdenum anode are observable in the continuous beam, K_α=17.48 KeV and K_β=19.61 KeV. Quasi-monochromatic beams and photon flux obtained are shown in Fig. 4.12 and reported in table 4.5 respectively.
Monochromatization efficiency of 26.7% is obtained.

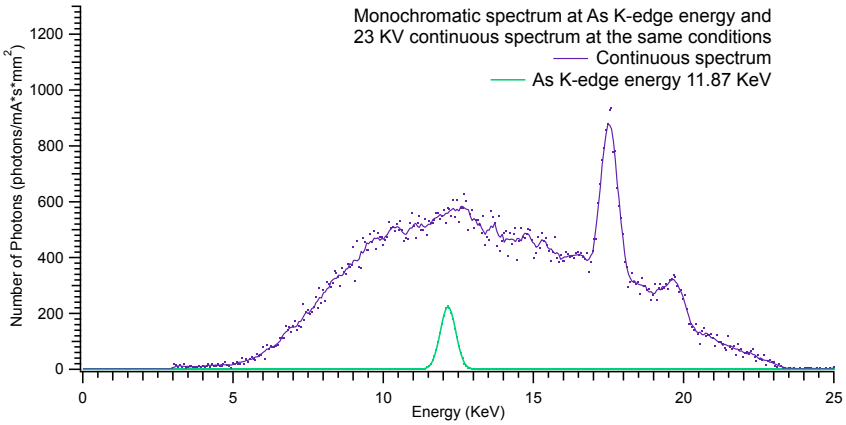

Figure 4.11: As: Bremsstrahlung spectrum at 23 KVp and monochromatic beam on K-edge energy

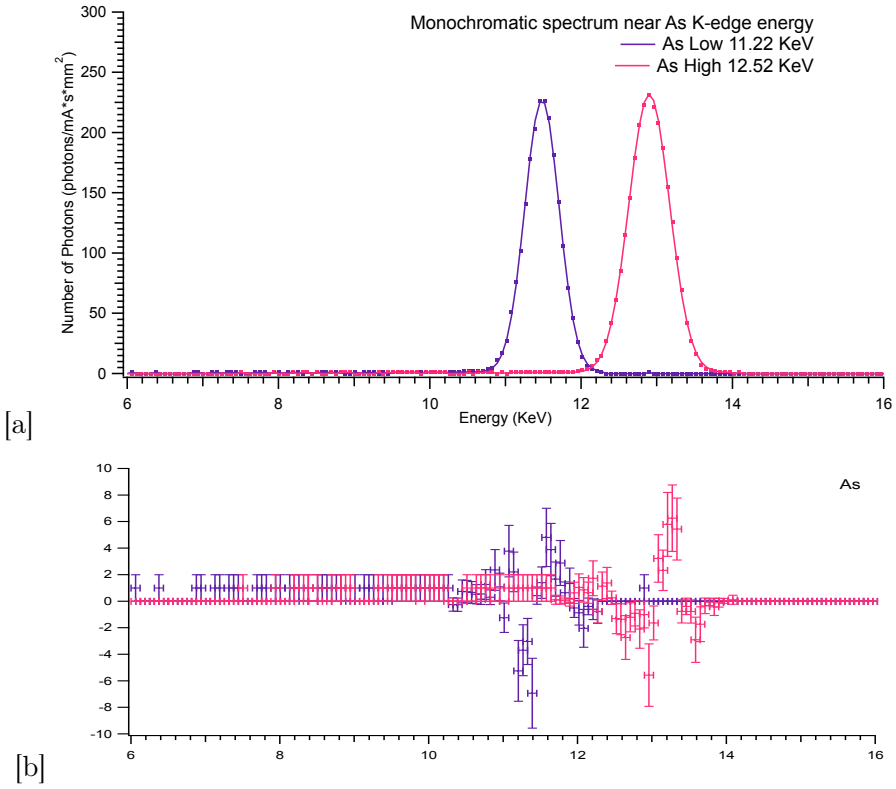

Figure 4.12: As: [a] monochromatic beam on energies bracketing K-edge energy and [b] residuals relative to the gaussian fit

As	**Setting Energy** KeV	x_0 KeV	**FWHM** KeV	**Flux** $ph/mm^2 * mA * s$
K-edge	11.87	12.16	0.43	2307 $\pm$48
Low	11.22	11.48	0.38	2085 $\pm$46
High	12.52	12.90	0.45	2522 $\pm$50

Table 4.5: Characteristics of the diffracted beams on Arsenic K-edge energy.

4.8 Bromine K-edge: 13.79 KeV

Measurement on Bromine K-edge energy has been realized with 26 KVp. Quasi-monochromatic beams and photon flux obtained are shown in Fig. 4.14 and reported in table 4.6 respectively.
Monochromatization efficiency of 32.5% is obtained.

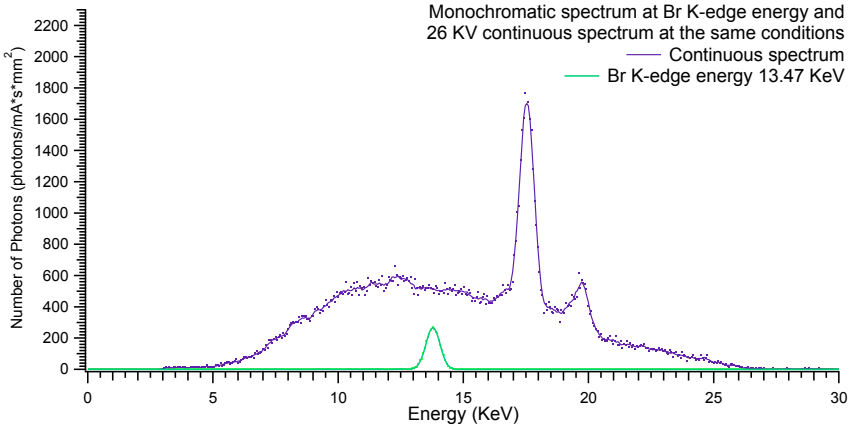

Figure 4.13: Br: Bremsstrahlung spectrum at 26 KVp and monochromatic beam on K-edge energy

Br	**Setting Energy** KeV	x_0 KeV	**FWHM** KeV	**Flux** $ph/mm^2 * mA * s$
K-edge	13.47	13.78	0.47	3003 ±55
Low	12.82	13.09	0.46	3147 ±56
High	14.12	14.38	0.46	3134 ±56

Table 4.6: Characteristics of the diffracted beams on Bromine K-edge energy.

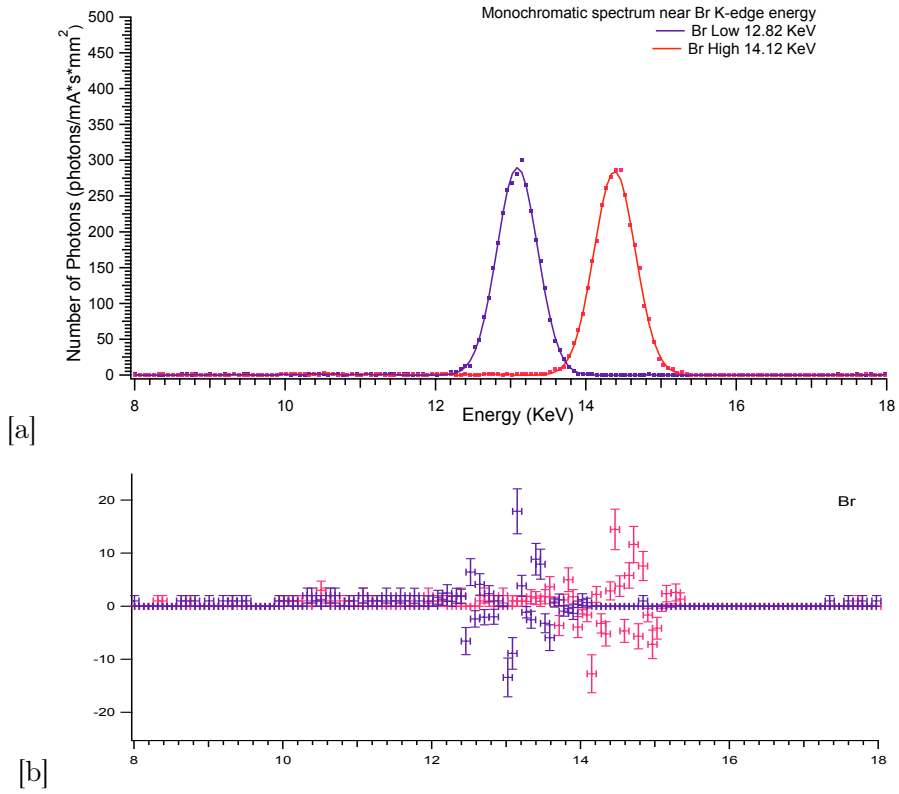

Figure 4.14: Br: [a] monochromatic beam on energies bracketing K-edge energy and [b] residuals relative to the gaussian fit

4.9 Strontium K-edge: 16.20 KeV

Measurement on Strontium K-edge energy has been realized with 31 KVp.
An increase energy distance between monochromatic beams energy is used to prevent beams overlap. Low and high spectra have been acquired at E_{-}=15.2 KeV and E_{+}= 17.20 KeV.
In Fig. 4.15 are shown monochromatic beams. As also reported in 4.8 a great photon flux disparity from the *low* and *high* energy beams is identified.
This is due by the influence of the K_{α} emission peak of the Mo anode at 17.40 KeV.
Monochromatization efficiency at Strontium K-edge energy is 5.9%.

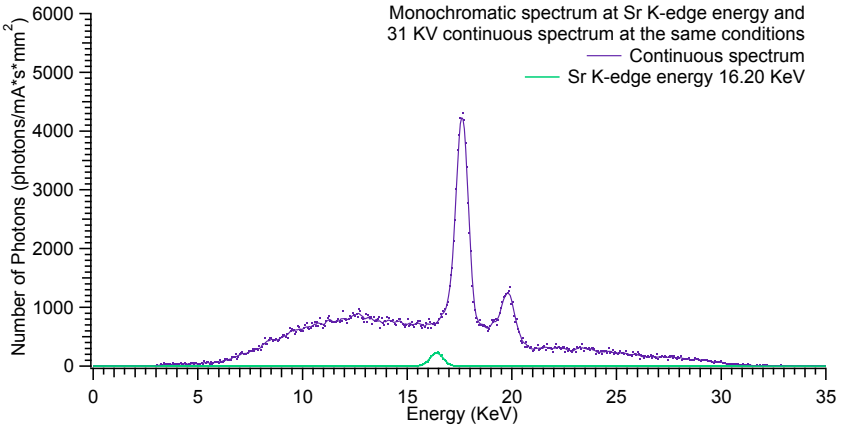

Figure 4.15: Sr: Bremsstrahlung spectrum at 31 KVp and monochromatic beam on K-edge energy

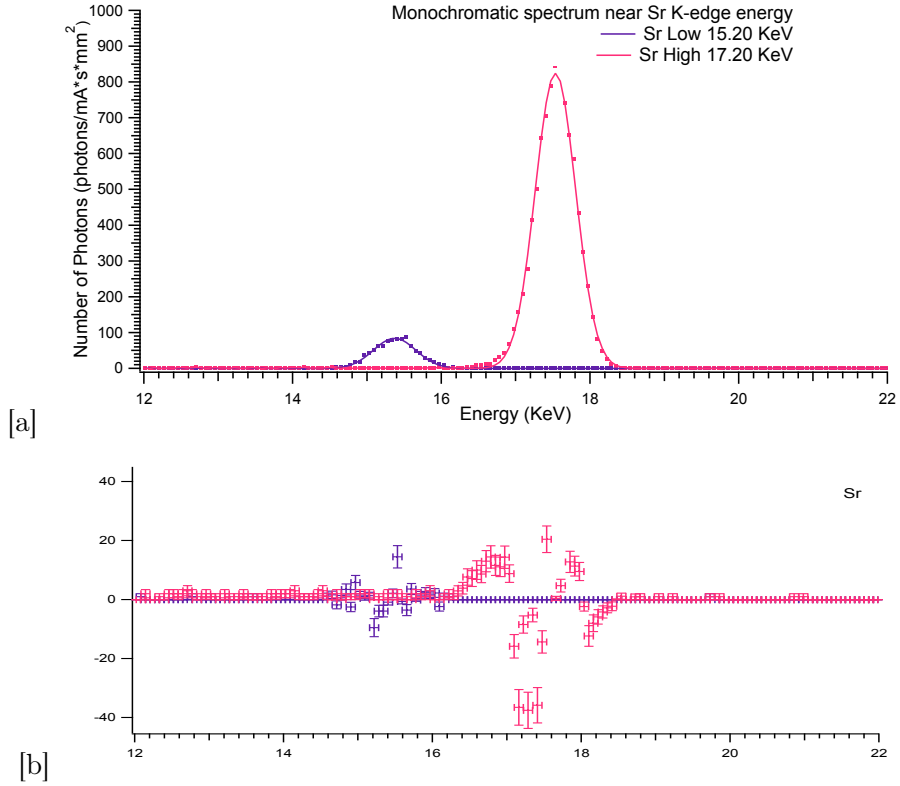

Figure 4.16: Sr: [a] monochromatic beam on energies bracketing K-edge energy and [b] residuals relative to the gaussian fit

Sr	Setting Energy KeV	x_0 KeV	FWHM KeV	Flux $ph/mm^2 * mA * s$
K-edge	16.20	16.40	0.53	2819 ±53
Low	15.20	15.37	0.47	957 ±31
High	17.20	17.53	0.45	8927 ±94

Table 4.7: Characteristics of the diffracted beams on Strontium K-edge energy.

4.10 Molybdenum K-edge: 19.99 KeV

At this energy, obtained with 36 KVp, K_β peak influence on monochromatic beam is massive.
Monochromatic beams at K-edge energy, 19.99 KeV, has almost the same energy of K_β anode emission, 19.61 KeV.
As shown in Fig 4.18 and reported in table 4.8 that comport a much higher photon flux, 16306 $\pm 127 ph/mm^2 \cdot mA \cdot s$, compared with flux at low and high energy, 6153 ± 78 and 3433 $\pm 59 ph/mm^2 \cdot mA \cdot s$ respectively.
At this energies spread of the beams, about 0.51 KeV, made necessary an energy separation increase, 2 KeV.
Monochromatization efficiency of 42.7% is obtained.

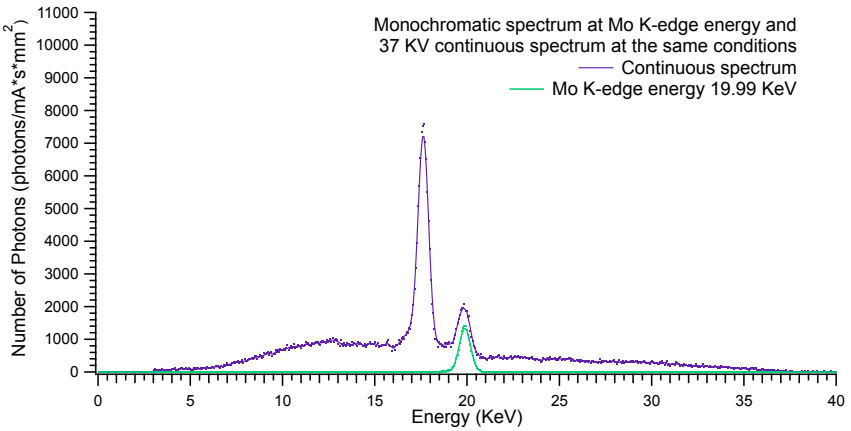

Figure 4.17: Mo: Bremsstrahlung spectrum at 36 KVp and monochromatic beam on K-edge energy

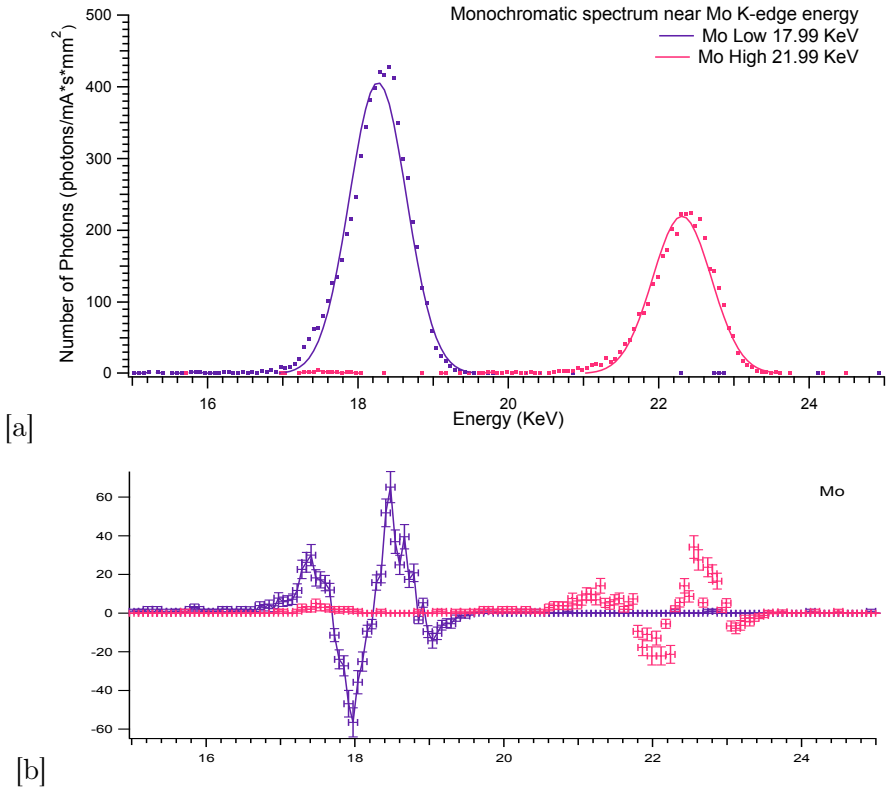

Figure 4.18: Mo: [a] monochromatic beam on energies bracketing K-edge energy and [b] residuals relative to the gaussian fit

Mo	**Setting Energy** KeV	x_0 KeV	**FWHM** KeV	**Flux** $ph/mm^2 * mA * s$
K-edge	19.99	19.87	0.51	16306 $\pm$127
Low	17.99	18.26	0.64	6153 $\pm$78
High	21.99	22.31	0.66	3433 $\pm$59

Table 4.8: Characteristics of the diffracted beams on Molybdenum K-edge energy.

4.11 Silver K-edge: 25.51 KeV

To realize measurement on Silver K-edge energy has been used maximum KVp achievable, 41 KVp.
As shown in Fig. 4.21 and reported in table 4.9 at this energies *low* energy beam present an higher flux than *high* energy, 4259 ±65 and 4075 ±64$ph/mm^2 \cdot mA \cdot s$ respectively.
Analyzing obtained spectrum (Fig. 4.20) a noise peaked in 4-5 KeV range is observed.
With traditional CCD this part of the flux cannot be delate. However by using a SSD this portion of the spectra can eliminated by threshold setting.
Monochromatization efficiency at this energy is 16.5%.

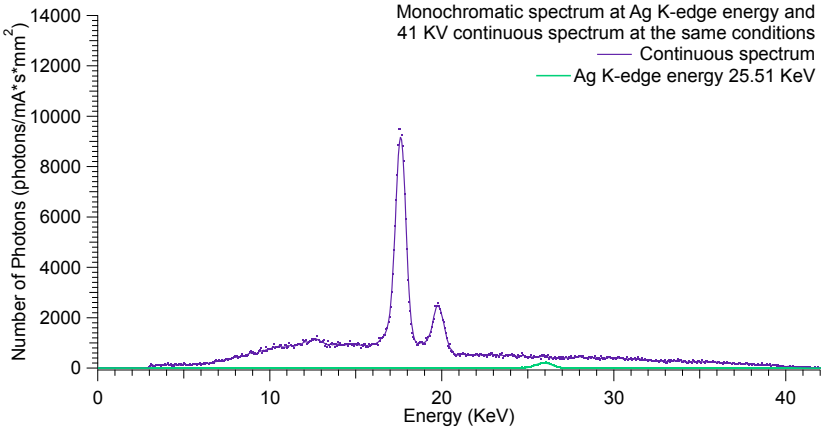

Figure 4.19: Ag: Bremsstrahlung spectrum at 41 KVp and monochromatic beam on K-edge energy

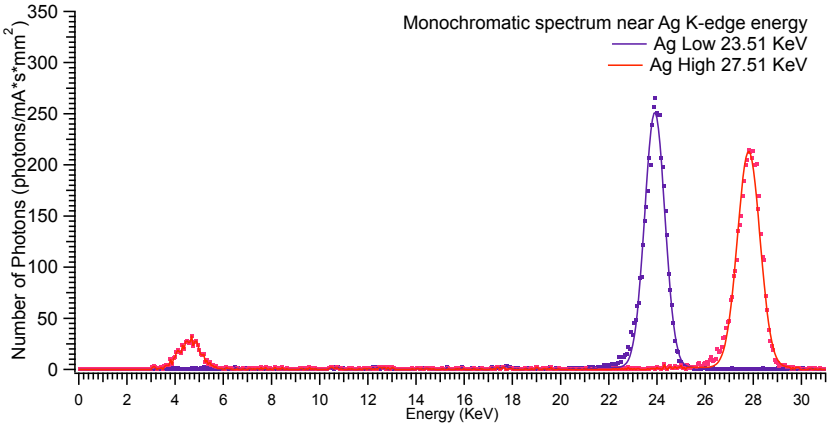

Figure 4.20: Monochromatic spectrum at Ag K-edge energy and noise detected

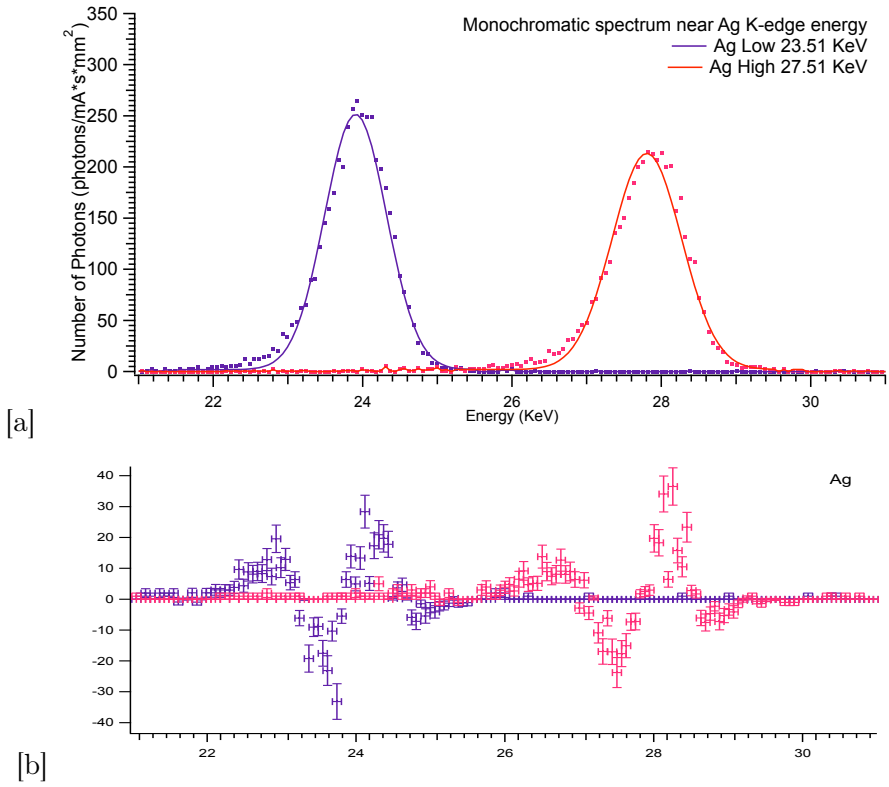

Figure 4.21: Ag: [a] monochromatic beam on energies bracketing K-edge energy and [b] residuals relative to the gaussian fit

Ag	**Setting Energy** KeV	x_0 KeV	**FWHM** KeV	**Flux** $ph/mm^2 * mA * s$
K-edge	25.51	25.93	0.79	4085 $\pm$64
Low	23.51	23.91	0.70	4259 $\pm$65
High	27.51	27.80	0.78	4075 $\pm$64

Table 4.9: Characteristics of the diffracted beams on Silver K-edge energy.

4.12 Cadmium K-edge: 26.71 KeV

To realize measurement on Cadmium K-edge energy has been used 41 KVp. As shown in Fig 4.23 also in this analysis the noise is observed. Monochromatic beams and photon flux obtained are shown in Fig. 4.24 and reported in table 4.10. Monochromatization efficiency of 14.8% is observed.

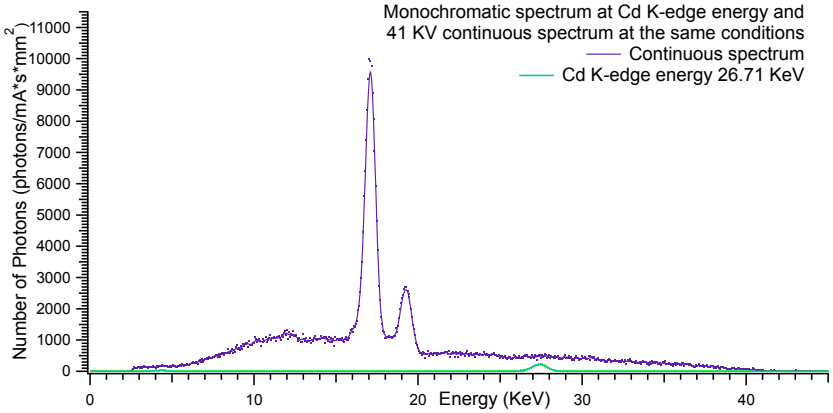

Figure 4.22: Cd: Bremsstrahlung spectrum at 41 KVp and monochromatic beam on K-edge energy.

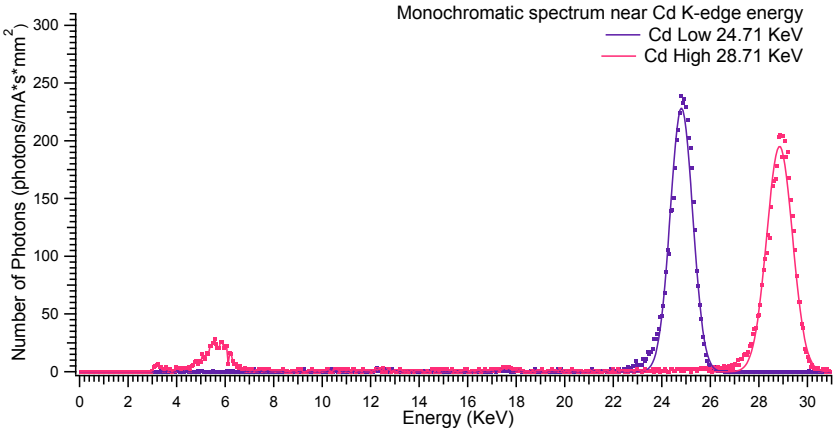

Figure 4.23: Monochromatic spectrum at Cd K-edge energy and noise detected.

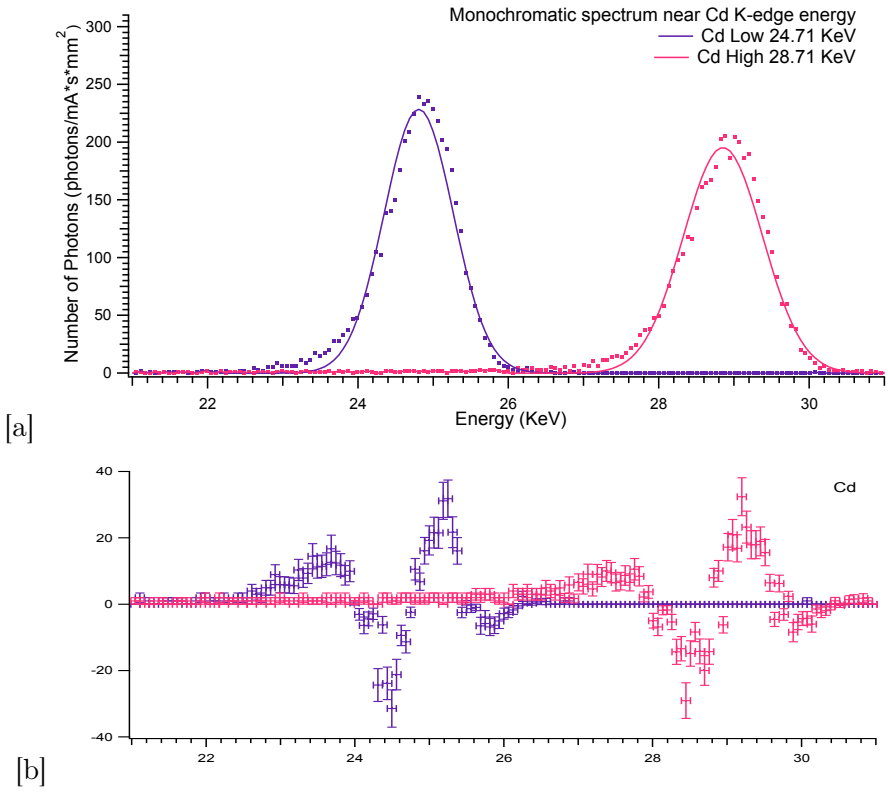

Figure 4.24: Cd: [a] monochromatic beam on energies bracketing K-edge energy and [b] residuals relative to the gaussian fit

Cd	**Setting Energy** KeV	x_0 KeV	**FWHM** KeV	**Flux** $ph/mm^2 * mA * s$
K-edge	26.71	27.38	0.80	4163 ±65
Low	24.71	24.81	0.77	4205 ±65
High	28.71	28.85	0.88	4117 ±64

Table 4.10: Characteristics of the diffracted beams on Cadmium K-edge energy.

4.13 Tin K-edge: 29.20 KeV

Also to realize measurement on Tin K-edge energy has been used 41 KVp and, as is shown in Fig.4.26, the low energy noise is observed.
Monochromatic beams and photon flux obtained are shown in Fig. 4.27 and reported in table 4.11.
Monochromatization efficiency of 3.2% is obtained.

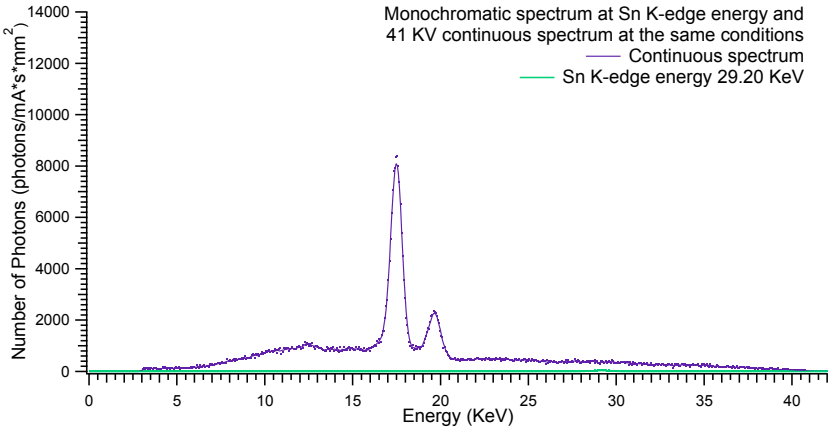

Figure 4.25: Sn: Bremsstrahlung spectrum at 41 KVp and monochromatic beam on K-edge energy

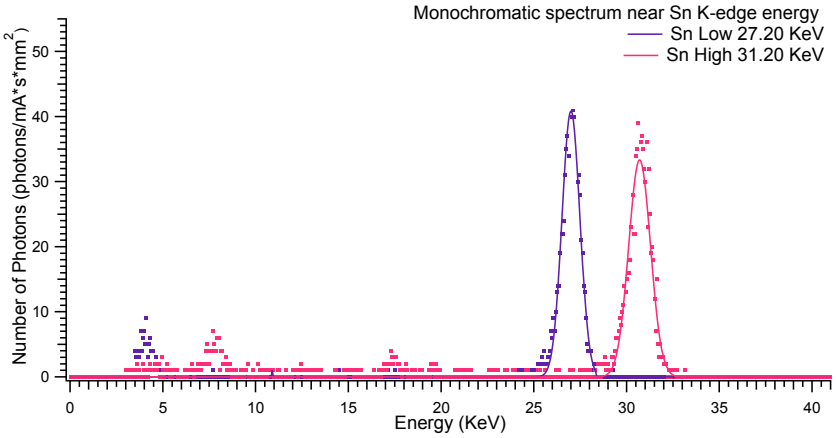

Figure 4.26: Monochromatic spectrum at Sn K-edge energy and noise detected.

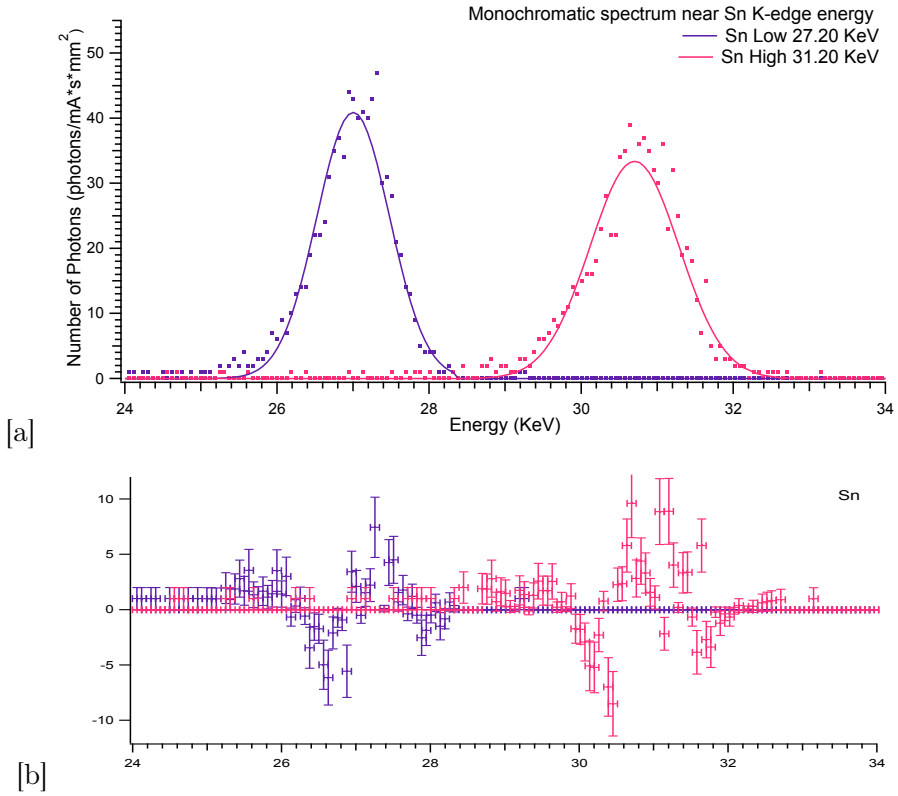

Figure 4.27: Sn: [a] monochromatic beam on energies bracketing K-edge energy and [b] residuals relative to the gaussian fit

Sn	**Setting Energy** KeV	x_0 KeV	**FWHM** KeV	**Flux** $ph/mm^2 * mA * s$
K-edge	29.20	29.07	0.88	818 $\pm$29
Low	27.20	27.00	0.80	781 $\pm$28
High	31.20	30.70	0.98	783 $\pm$28

Table 4.11: Characteristics of the diffracted beams on Tin K-edge energy.

4.14 Barium K-edge: 37.44 KeV

To realize measurement on Barium K-edge energy has been used 41 KVp. As shown in Fig.4.26 Bremsstrahlung shape is recognizable, probably due to a non-perfect collimation of the source.
At this energy Bragg diffraction requires small angles and a fraction of the primary beam impinging on the detector. Emission peaks of the source are distinguishable. To perform K-edge radiography on Barium CCD is not usable and SSD became indispensable.
Monochromatic beams and photon flux obtained are shown in Fig. 4.30 and reported in table 4.12.
At this energy monochromatization efficiency of 2.5% is obtained.

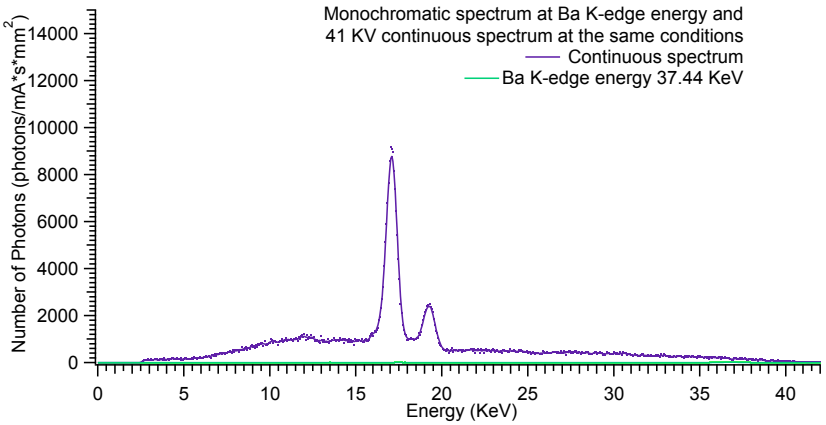

Figure 4.28: Ba: Bremsstrahlung spectrum at 41 KVp and monochromatic beam on K-edge energy

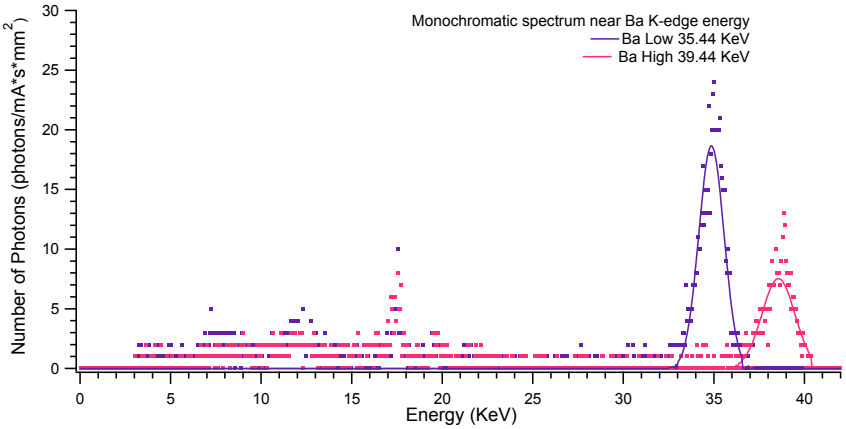

Figure 4.29: Monochromatic spectrum at Ba K-edge energy and fraction of the non-diffracted beam

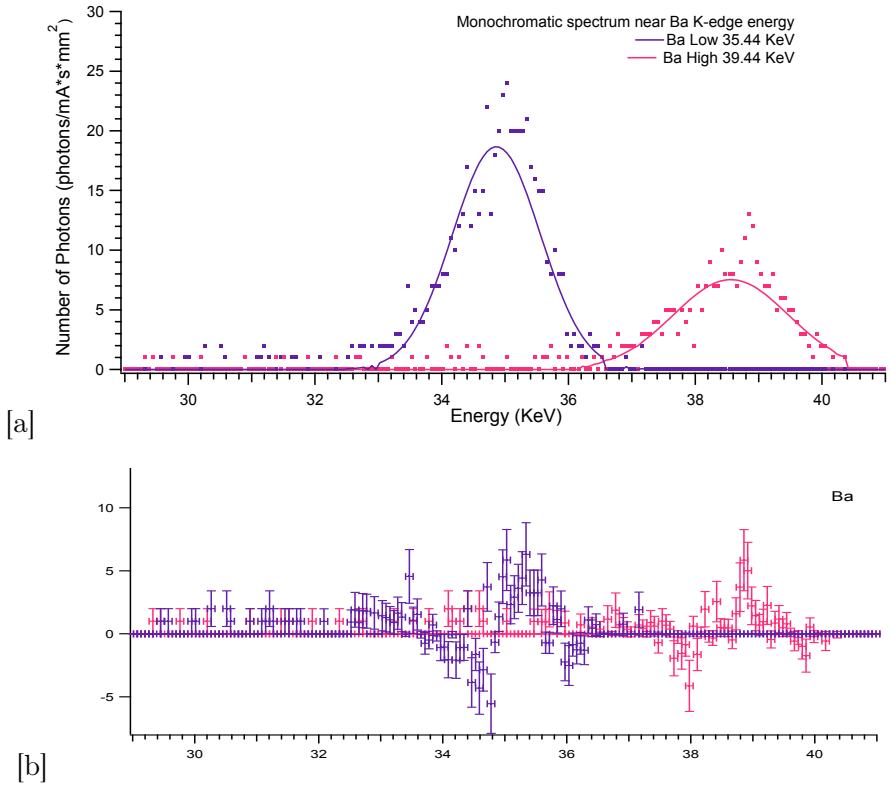

Figure 4.30: Ba: [a] monochromatic beam on energies bracketing K-edge energy and [b] residuals relative to the gaussian fit

Ba	**Setting Energy** KeV	x_0 KeV	**FWHM** KeV	**Flux** $ph/mm^2 * mA * s$
K-edge	37.44	36.77	1.07	420 ±20
Low	35.44	34.86	1.16	514 ±23
High	39.44	38.56	1.53	258 ±16

Table 4.12: Characteristics of the diffracted beams on Barium K-edge energy.

		Setting Energy KeV	x_0 KeV	**FWHM** KeV	**Flux** $ph/mm^2 * mA * s$
Fe	**Low**	6.46	6.54	0.34	56 ±7
	High	7.76	7.92	0.38	211 ±15
Co	**Low**	7.06	7.26	0.46	99 ±10
	High	8.36	8.51	0.46	333 ±18
Cu	**Low**	8.33	8.48	0.33	497 ±22
	High	9.63	9.82	0.40	781 ±28
Zn	**Low**	9.00	9.26	0.42	708 ±27
	High	10.30	10.52	0.40	1098 ±33
As	**Low**	11.22	11.48	0.38	2085 ±46
	High	12.52	12.90	0.45	2522 ±50
Br	**Low**	12.82	13.09	0.46	3147 ±56
	High	14.12	14.38	0.46	3134 ±56
Sr	**Low**	15.20	15.37	0.47	957 ±31
	High	17.20	17.53	0.45	8927 ±94
Mo	**Low**	17.99	18.26	0.64	6153 ±78
	High	21.99	22.31	0.66	3433 ±59
Ag	**Low**	23.51	23.91	0.70	4259 ±65
	High	27.51	27.80	0.78	4075 ±64
Cd	**Low**	24.71	24.81	0.77	4205 ±65
	High	28.71	28.85	0.88	4117 ±64
Sn	**Low**	27.20	27.00	0.80	781 ±28
	High	31.20	30.70	0.98	783 ±28
Ba	**Low**	35.44	34.86	1.16	514 ±23
	High	39.44	38.56	1.53	258 ±16

Table 4.13: Summary table of the characteristics of the analyzed diffracted beams.

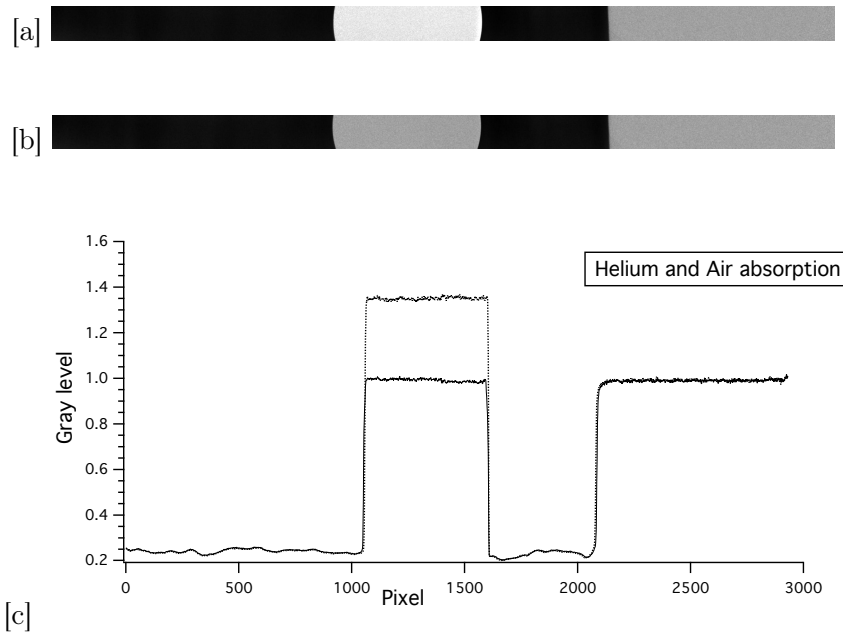

Figure 4.29: Images of the X-ray beam through air [a] and helium flux [b]. Average gray level, by column, of the previous images.

4.15 Air attenuation

In this energy range, 7-27 KeV, air attenuation reduces strongly the photon flux. An helium box surrounding the K-edge facility has been tested to get the photon flux. A plexiglass tube, about 50 cm long, with two thin mylar windows, fluxed by helium gas, has been used to simulate an helium box. The same tube, open to air, has been used to realize a second image.
The test has been performed with the CCD detector at 10 KeV beam energy.
In Fig.4.29[a,b] image results of air and helium, after dark current and white field corrections, are shown.
Darker part of the images shown the tube support, the central part represent the inside of the tube, fluxed by Helium [a] or open to air [b]. On the right side is shown the outside air atmosphere. To allow the best visual comparison, images are presented with same luminosity and contrast settings.
Previous images have been normalized and average for columns of pixels have been calculated and presented in Fig.4.29. Reduced photon absorption due to helium atmosphere is highlighted and a photon flux increment of 36% has been measured.

Chapter 5

K-edge imaging

K-edge radiography has been performed on different test objects, realized by the *Cultural Heritage Restoration and Conservation Center "La Venaria Reale"* [1], in Turin, Italy.
These samples have been made with two main aims: test the system capability to quantify elements content in the target and identify different superimposed layers for a list of selected pigments.
Objects with two different typologies have been realized, both on small canvas, 10×10 cm. Some of them are divided in five section with an increasing number of layers of the same pigment, as shown in Fig.5.1[a]. In the second type two different pigments have been used and, in the central part of canvas, they have been superimposed as shown in Fig.5.1[b]. Other smaller target object, 3×3 cm, have been realized with different pigment, in linseed oil and on a mylar support.

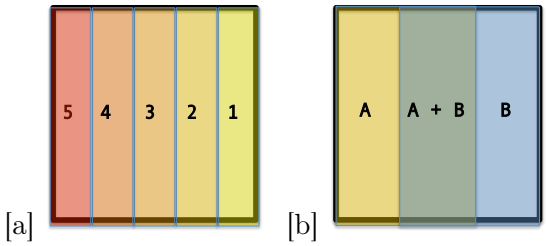

Figure 5.1: Target object structure

[1] Courtesy of A.Giovagnoli, M. Nervo e P. Buscaglia,
Cultural Heritage Restoration and Conservation Center "La Venaria Reale"

5.1 Iron

K-edge radiography has been made to detect Iron distribution on different test objects on a mylar support.
The first of them has been carried out with a mixture of Azurite and Lead White pigment. The second one with Prussian Blue.
Both pigments were mixed with linseed oil as binder.
At the Iron K-edge energy, 7.11 KeV, our setup cannot produced only first order diffraction beam. Only SSD analysis is achievable; the second order diffraction may be erased by a suitable choice of threshold in the detector read-out.
Low and High images have been acquired at energies E_{-}=6.46 KeV and E_{+}=7.76 KeV respectively, 16 KVp and 56.5 mAs.
In Fig.5.2[a] results of SSD mapping are shown.
These image represent, according to the Lehmann algorithm, the element distribution in g/cm^2 on the analyzed surfaces; higher grey level correspond to a greater quantity of the element under study, Iron in these samples.
The dark area on the right, on Prussian Blue pigment, is a lower Iron quantity linked to thinner pigment layer.
In Fig.5.2[b] the average Fe content in each pixel column is shown. In Fig.5.2[c] the Iron mean values in the sample are displayed. Error bars are the standard deviation of the mean Iron content.
Both pigments present Iron content, also confirmed by non quantitative XRF analysis carried out by "Venaria Reale" (Fig.5.4).

To get an estimate of the systematic background in this quantitative measurements the same procedure has been followed with different object. The same Prussian Blue object displayed on the right, and a ground sheet (mylar) on the left. Results are shown in Fig.5.3 where it is clearly possible to discriminate Iron content from its absence in mylar. The residual level of 0.003 g/cm^2 detected is the background size in the measurements.

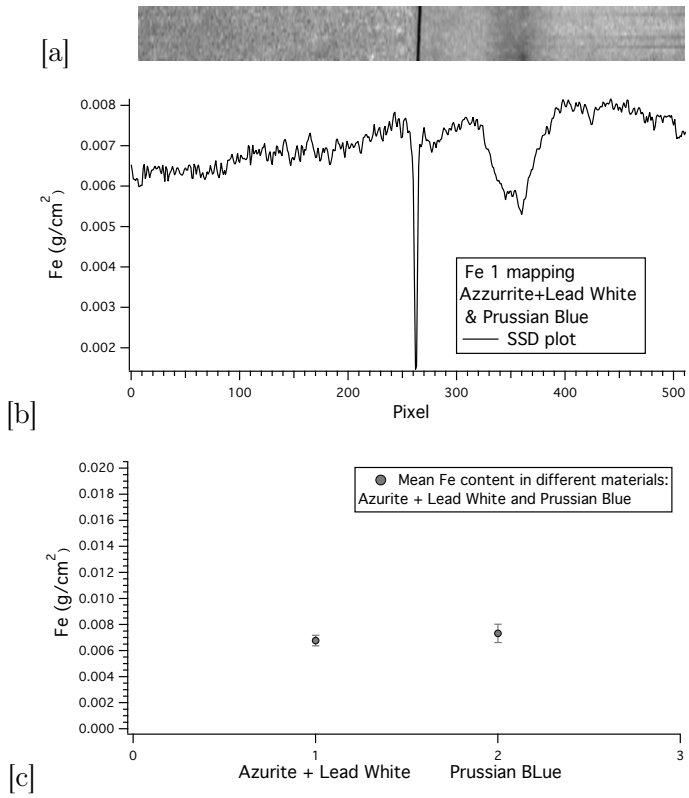

Figure 5.2: Images of Iron distribution; [a] Fe content (g/cm^2) detected in Azurite and Lead White (on the left) and Prussian Blue (on the right) target object; [b] average Iron content by column obtained on all map; plot [c] represents mean Iron content detected in each object.

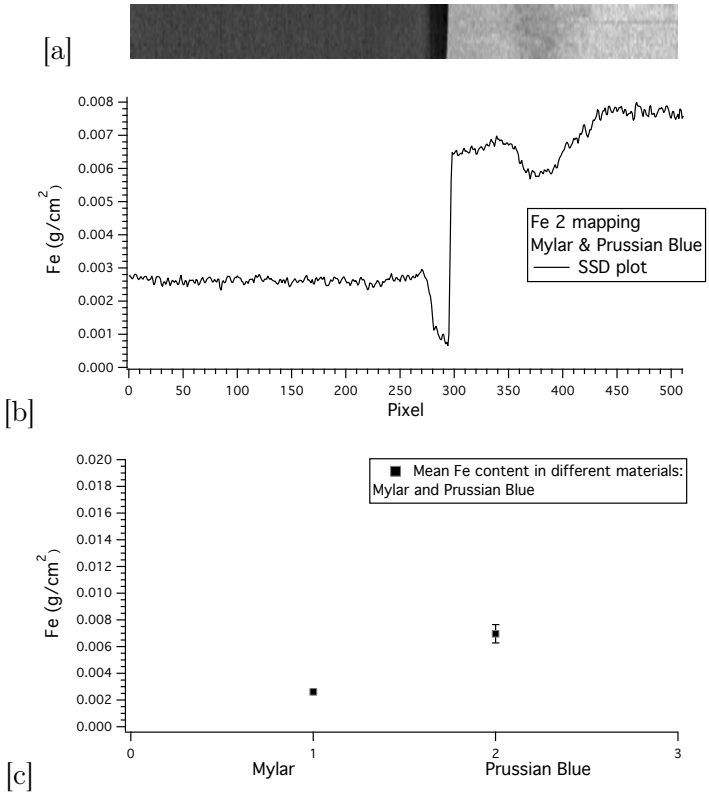

Figure 5.3: Images of Iron distribution; [a] Fe content (g/cm^2) detected in the equivalent absorber (on the left) and Prussian Blue (on the right) target object; [b] average Iron content by column obtained on all map; plot [c] represents mean Iron content detected

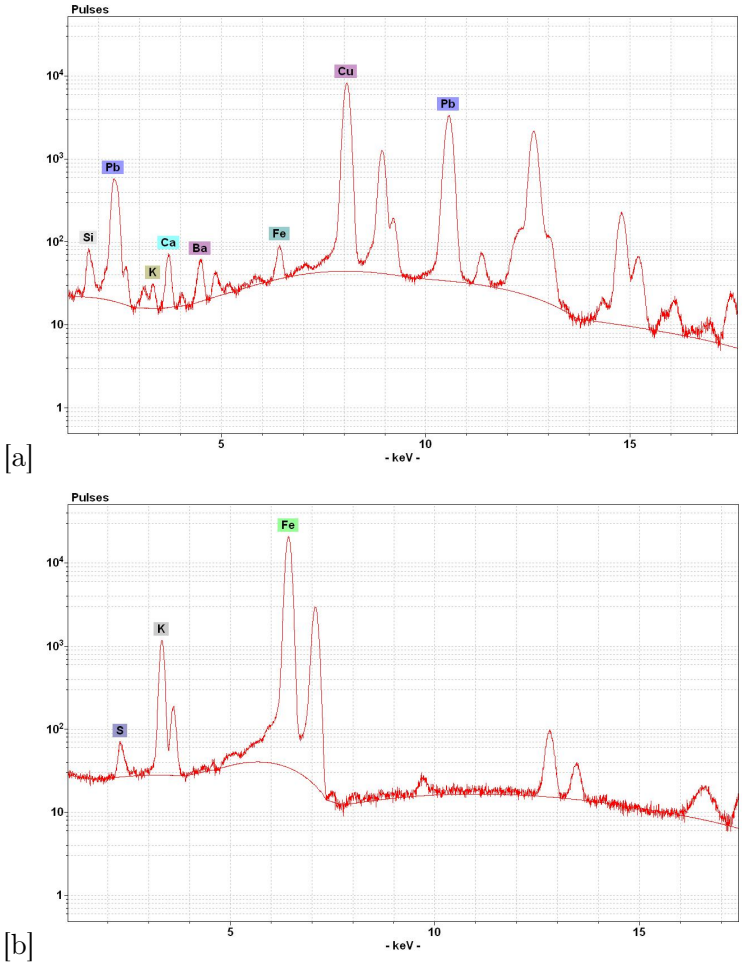

Figure 5.4: XRF analysis performed on target object: Azurite and Lead White [a] and Prussian Blue [b]

5.2 Cobalt

Same test objects type described above have been used to perform K-edge radiography for Cobalt distribution.
Two pigment samples have been used: on the right Azurite pigment and, on the left, Smaltino. Like previous object pigments were mixed with linseed oil as binder and on a mylar support.
Images have been acquired at energies E_-=7.06 KeV and E_+=8.36 KeV respectively, 16 KVp and 56.5 mAs.
In Fig. 5.5[a] results of SSD mapping are shown. Only on the right part of the image, in Smaltino, Cobalt is detected.
In Fig. 5.5[b] the average Co content in each pixel column is shown. In Fig. 5.5[c] the Cobalt mean values in the sample are displayed. Error bars are the standard deviation of the mean Cobalt content.
XRF analysis performed confirm K-edge mapping results (Fig.5.6).

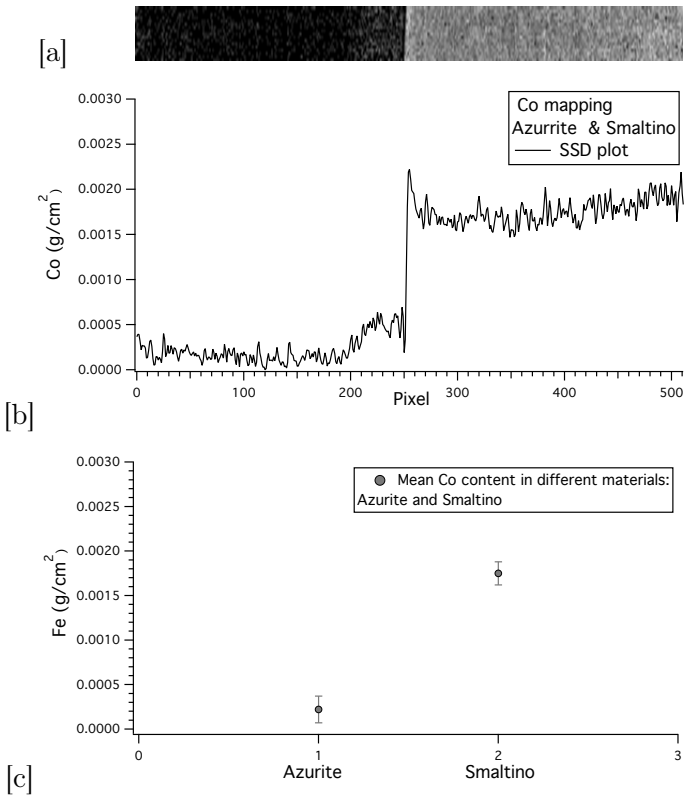

Figure 5.5: Images of Cobalt distribution; [a] Co content (g/cm^2) detected in the Azurite (on the left) and Smaltino (on the right) target object; [b] average Cobalt content by column obtained on all map; plot [c] represents mean Cobalt content detected.

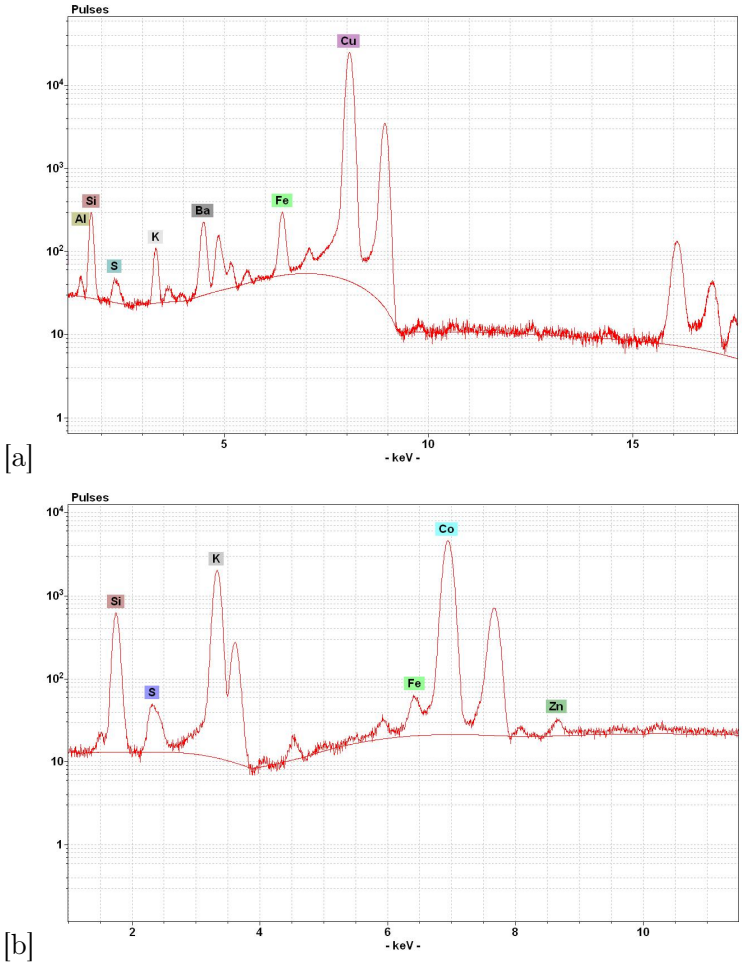

Figure 5.6: XRF analysis performed on target object: Azurite [a] and Smaltino [b]

5.3 Copper

Same test objects analyzed in previous section have been used to perform K-edge radiography for Copper distribution.
Images have been acquired at energies E_-=8.33 KeV and E_+=9.63 KeV respectively, 18 KVp and 56.5 mAs.
As aspected Copper content is detected only in the Azurite target object (Fig.5.7).
XRF analysis shown above confirm K-edge mapping results (Fig.5.6).

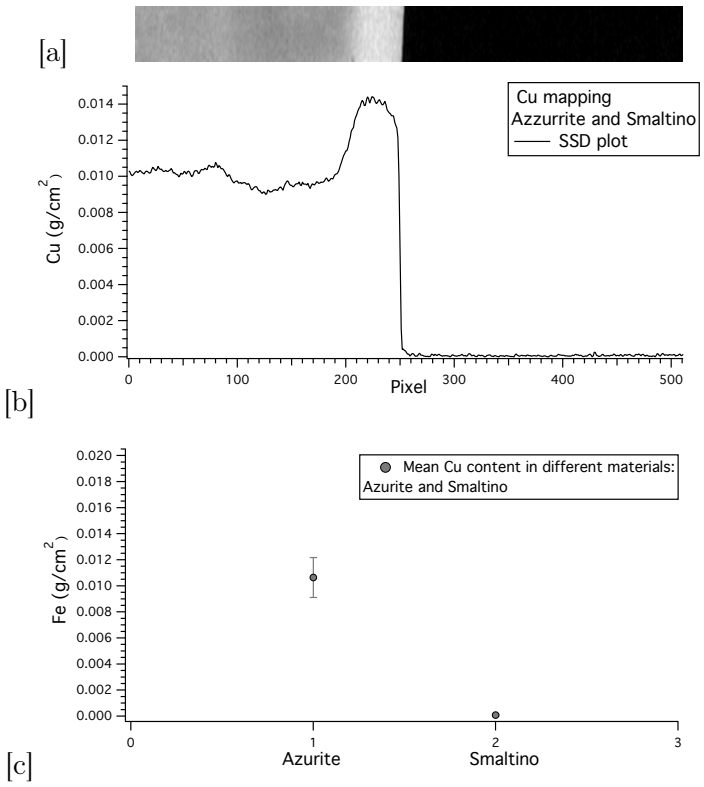

Figure 5.7: Images of Copper distribution; [a] Cu content (g/cm^2) detected in the Azurite (on the left) and Smaltino (on the right) target object; [b] average Copper content by column obtained on all map; plot [c] represents mean Copper content detected

5.4 Zinc

K-edge radiography has been applied on target object type [a] as illustrated in Fig.5.1.
Objects have been composed of an increasing number of superimposed pigment layers of Zinc White (ZnO, Kremer Pigments[2], n.46300). The painting color has been realized with a pigment proportion of 1.5 g of ZnO in 2.5 g of binder.
Images have been acquired at E_-=9.00 KeV and E_+=10.30 KeV respectively.
CCD images have been realized using 20 KVp and 362.5 mAs.
On the other hand SSD imaging may be obtained at higher KVp because the second order diffraction may be erased by a suitable choice of threshold in the detector read-out. For this measure have been used 25 KVp and 113 mAs.
The large CCD detection area has made easy the mapping the whole target. The SSD small dimensions allow only the analysis of a small fraction of the sample. The central part of the target has been chosen for the SSD imaging, focusing the analysis on target side where element content is lower, i.e. from single layer to four superimposed layers.
In Fig.5.8 results of both mappings in terms of g/cm^2 of Zinc detected are shown. To allow the best visual comparison, images are presented with same luminosity and contrast.
It is clearly possible to identify each layer, both for CCD and SSD images. Because of the great difference between the thickness of the canvas and wooden frame the test object's frame is often visible in the images acquired with the CCD detector.
In Fig.5.9 the average for columns of pixels of the previous images are compared.
The plot in Fig.5.10 represents the Zinc mean values in g/cm^2 for the four different layers obtained in CCD and SSD analysis. Error bars, which are the standard deviation of the mean Zinc content of the layer, are mainly due to the canvas texture. Since the thickness of the layers has been uncontrolled a non-complete linearity of Zinc content with layers number is highlighted.
Plots show a fairly good compatibility between CCD and SSD measurements.

[2]Kremer Pigmente, GmbH & Co. KG, Aichstetten, Germany

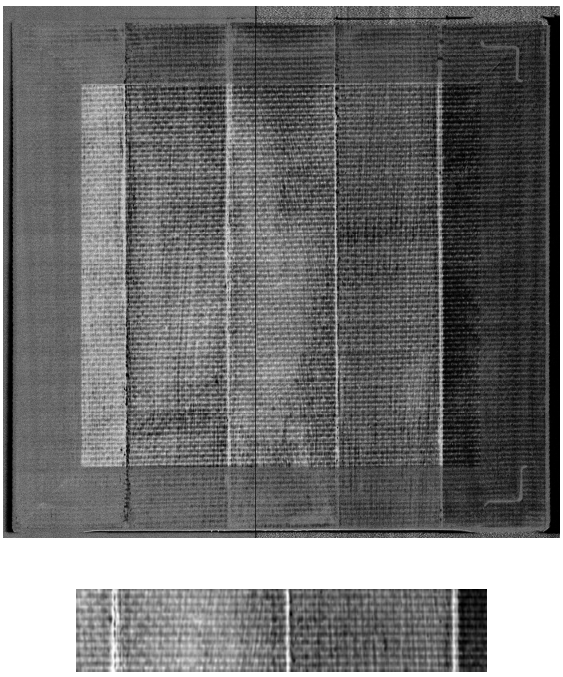

Figure 5.8: Images of Zinc distribution; Zn content (g/cm^2) detected by CCD (above) and SSD (below)

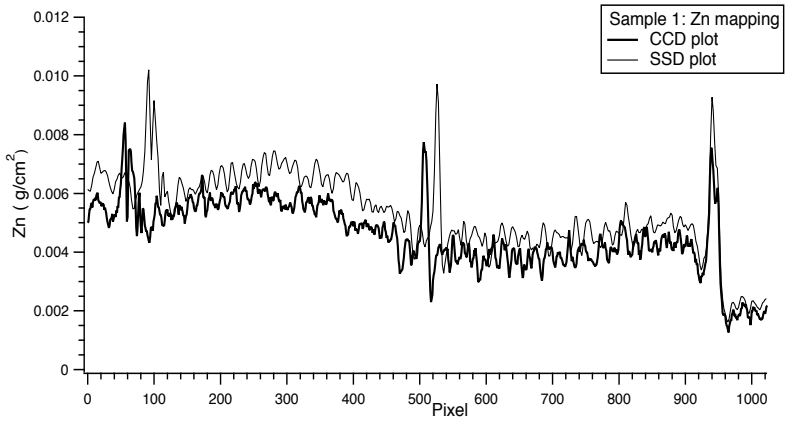

Figure 5.9: Average Zinc content by column obtained on all SSD map and the corresponding region on CCD image

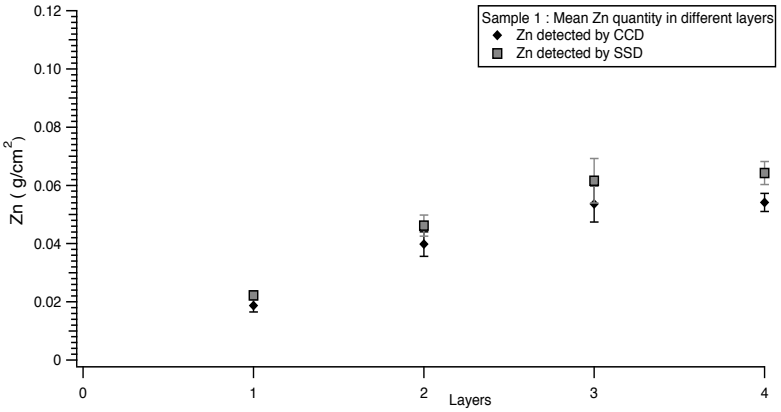

Figure 5.10: Mean Zinc content detected in each layer

5.5 Arsenic

Radiographic images to investigate Arsenic have been acquired at energies at E_-=11.22 KeV and E_+=12.52 KeV respectively.
For CCD images 23 KV and 565 mAs have been used.
Imaging with SSD has been performed with 25 KVp and 113 mAs.
The target object has an increasing number of superimposed pigment layers of Realgar (As_2S_2, Kremer pigments, n.10800) on canvas. The painting color has been realized with a pigment proportion of 2.2 g of As_2S_2 in 2.9 g of binder.
Painting layers are not homogenous and this problem is highlighted with K-edge mapping, shown in Fig.5.11. It is possible to identify single pigment thickening connected to little aggregates of pigment on the canvas texture.
The average for columns of pixels in Fig.5.12 reflects the inhomogeneity in the painting layers. Furthermore the analysis have highlighted that the Arsenic content don't increase linearly with layers number (Fig.5.13): homogenization difficulty has influenced the preparation of the test object.
However the CCD and SSD measurements have led to compatible results in terms of Arsenic content estimation.

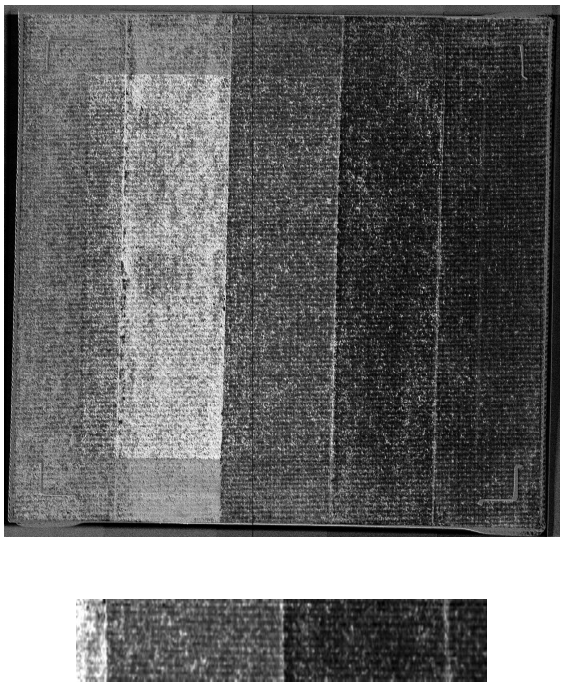

Figure 5.11: Images of Arsenic distribution; As content (g/cm^2) detected by CCD (above) and SSD (below)

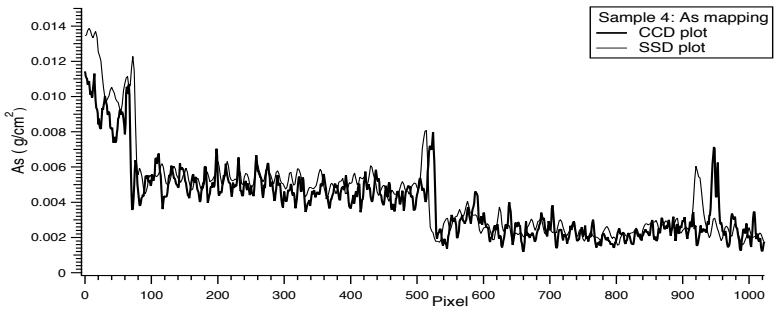

Figure 5.12: Average Arsenic content by column obtained on all SSD map and the corresponding region on CCD image

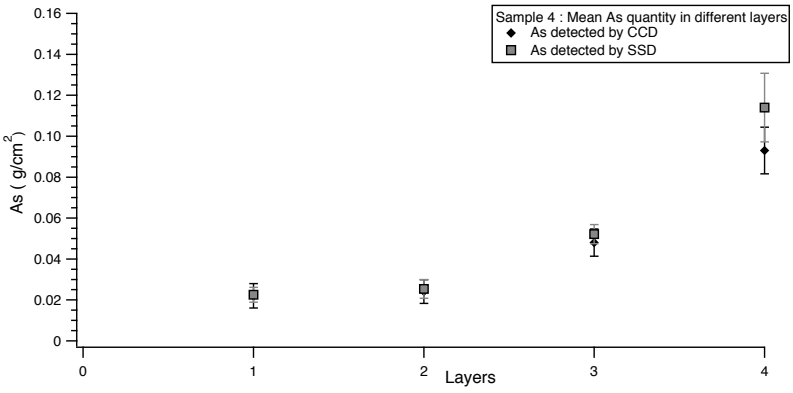

Figure 5.13: Mean Arsenic content detected in each layer

5.6 Cadmium

Radiographic images to investigate Cadmium have been acquired at energies E_-=24.71 KeV and E_+=28.71 KeV respectively and maximum achievable KVp is used, 41 KVp.
CCD images have been obtained with 431.5 mAs; with 86.3 mAs for SSD.
Target object with an increasing number of superimposed pigment layers, from 2 to 5, of Cadmium Red ($CdS + CdSe$, Kremer pigments n. 21140) has been analyzed. The painting colour has been realized with a pigment proportion of 2.1 g of powder in 2.4 g of binder.
A comparison between the K-edge mapping realized with CCD and SSD is shown in Fig.5.14. Due to low efficiency of the front-illuminated CCD detector at this energies, no Cadmium is detected by CCD (Fig. 5.15, 5.16).
Other target object has been realized with a different Cadmium Red pigment (Fig.5.18) and a different number of superimposed layers of pigments have been made: 3, 6 and 9.
This sample has been analyzed with SSD by using same energy, KVp and current settings of previous analysis.
Results obtained are shown in Fig.5.17. As expected a greater Cadmium content is detected. Standard deviations value, connected to canvas texture, does not allows to discriminate each layers.

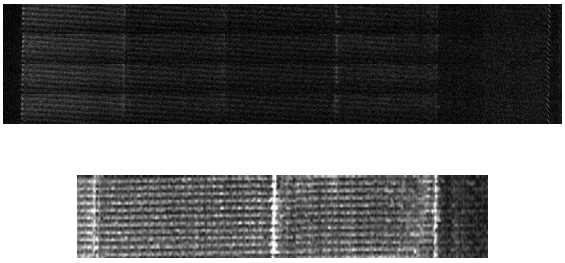

Figure 5.14: Images of Cadmium distribution; Cd content (g/cm^2) detected by CCD (above) and SSD (below)

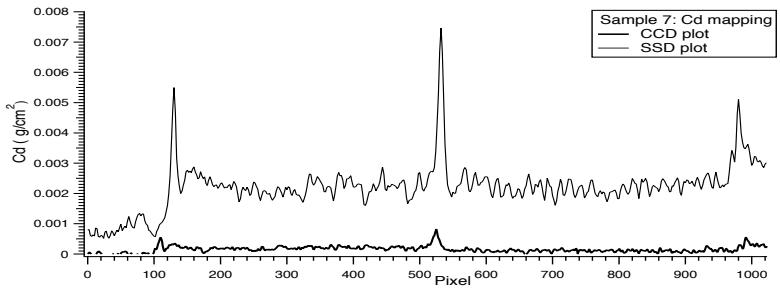

Figure 5.15: Average Cadmium content by column obtained on all SSD map and the corresponding region on CCD image

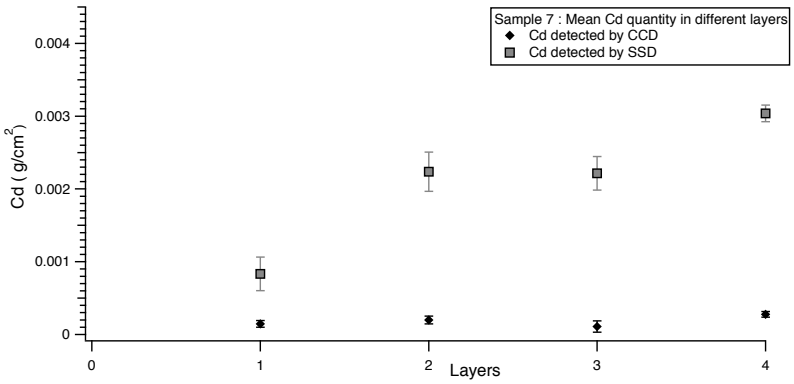

Figure 5.16: Mean Cadmium content detected in each layer

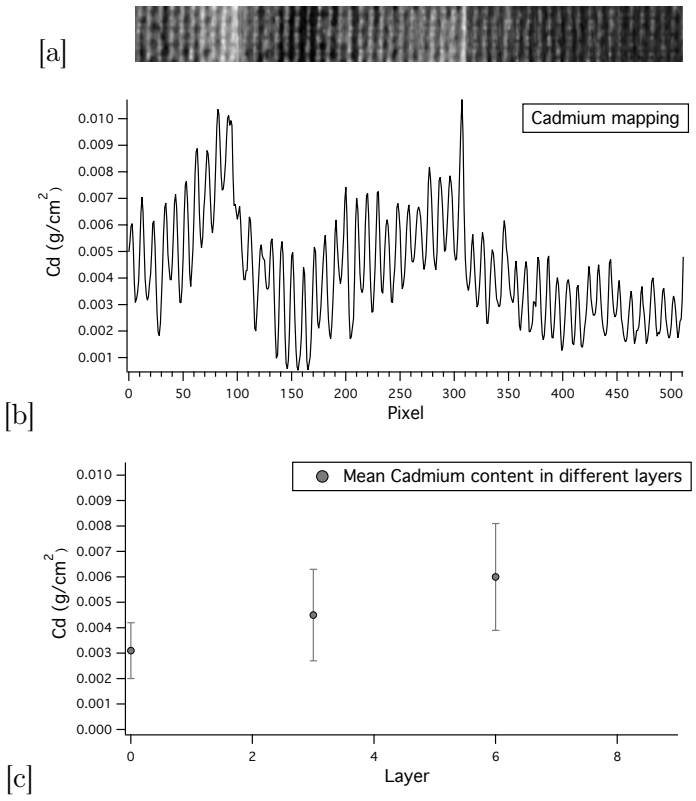

Figure 5.17: Images of Cadmium distribution; [a] Cd content (g/cm^2) detected in 3, 6 and 9 superimposed layers; [b] average Cadmium content by column obtained on all map; plot [c] represents mean Cadmium content detected

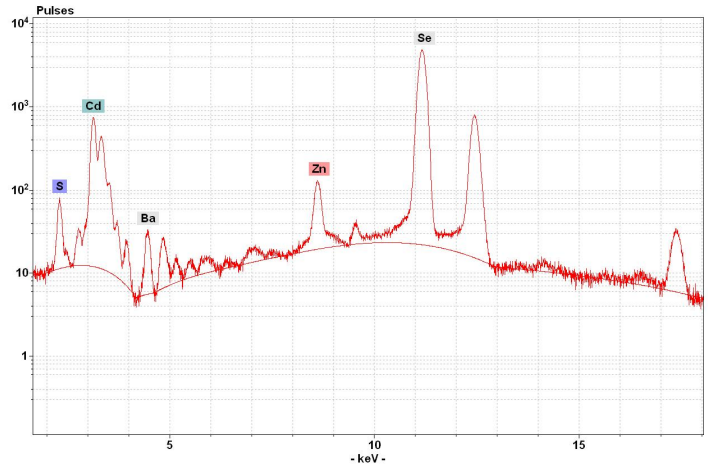

Figure 5.18: XRF analysis performed on Red Cadmium pigment

5.7 Tin

Similar test object analyzed in previous section has been realized using Lead and Tin Yellow pigment (Fig.5.20). Also a section of target object without pigment has been analyzed.
Images have been acquired using SSD detector, at energies E_{-}=27.00 KeV and E_{+}=30.70 KeV respectively, 41 KVp and 82.5 mAs.
Result is shown Fig.5.19[a] where it is possible to discriminate each part of target object. However, as highlighted in Fig.5.19[b], where the Tin average content in each pixel column is shown, Tin content are similar in each layer. The plot in Fig.5.19[c] represents the Tin mean values in g/cm^2 for each layers obtained by SSD analysis. Error bars, which are the standard deviation of the mean Tin content of the layer, are mainly due to the canvas texture.

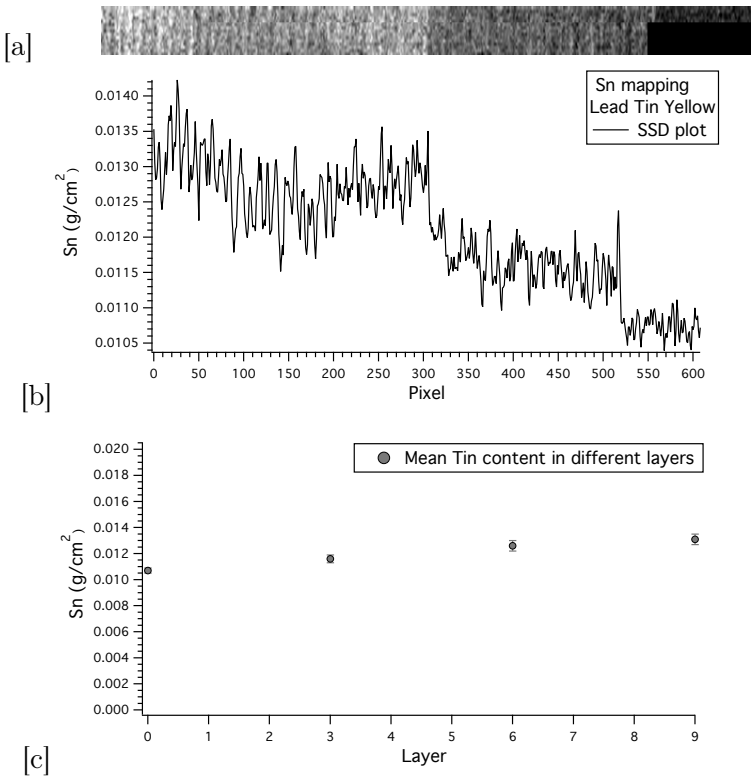

Figure 5.19: Images of Tin distribution; [a] Sn content (g/cm^2) detected on canvas and 3 and 6 superimposed layers; [b] average Tin content by column obtained on all map; plot [c] represents mean Tin content detected

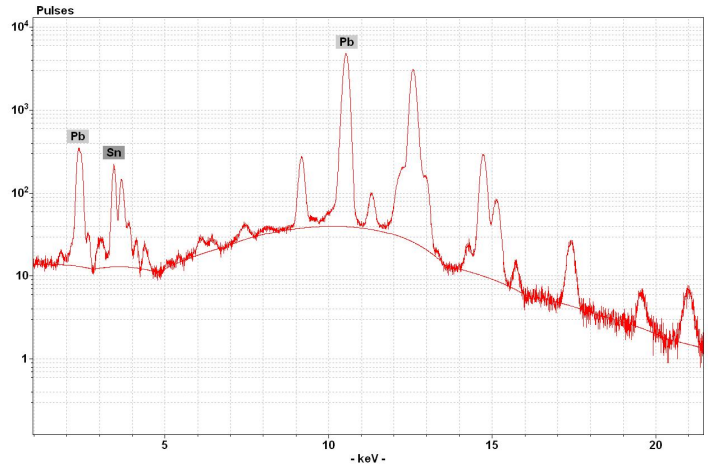

Figure 5.20: XRF analysis performed on Tin Lead Yellow pigment

5.8 More complex samples

A target object, where Cadmium Yellow ($CdS + ZnS$, Kremer pigments n. 21020) and Realgar (As_2S_2, Kremer pigments n.10800) have been superimposed in the central part, has been analyzed.
K-edge radiography on two different elements, Zinc and Arsenic, has been performed. The Zinc and Arsenic distributions are obtained with energies, KVp and current condition as in chapter 5.4 and 5.5. Zinc and Arsenic mapping are shown in Fig.5.21 and Fig.5.23 and show a good separation between the two pigments.
The Zinc and Arsenic contents obtained with CCD and SSD are presented in Fig.5.22 and Fig.5.24.
Due to the low CCD efficiency at this energies has been performed Cadmium mapping only with SSD detector 5.25.

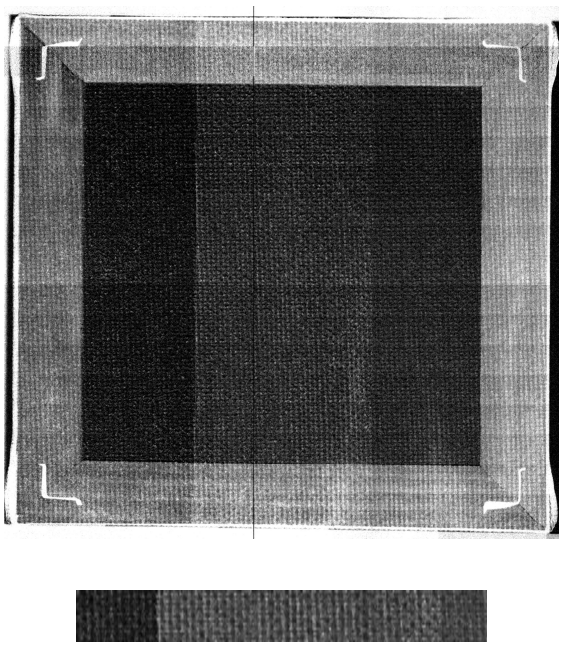

Figure 5.21: Mapping with CCD and SSD of Zinc distribution: the Zinc compound is on the right part of the sample

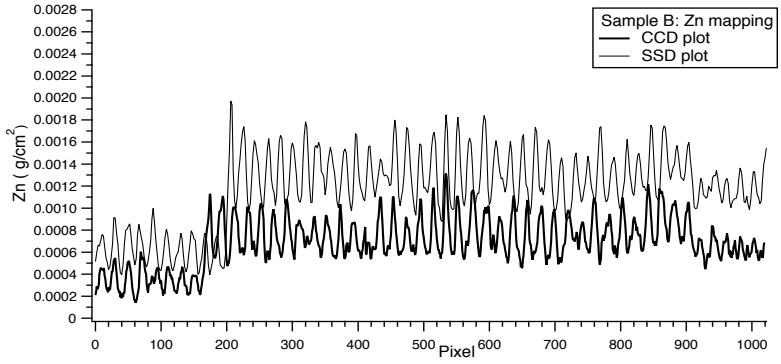

Figure 5.22: Average Zinc content by column obtained on all SSD map and the corresponding region on CCD image

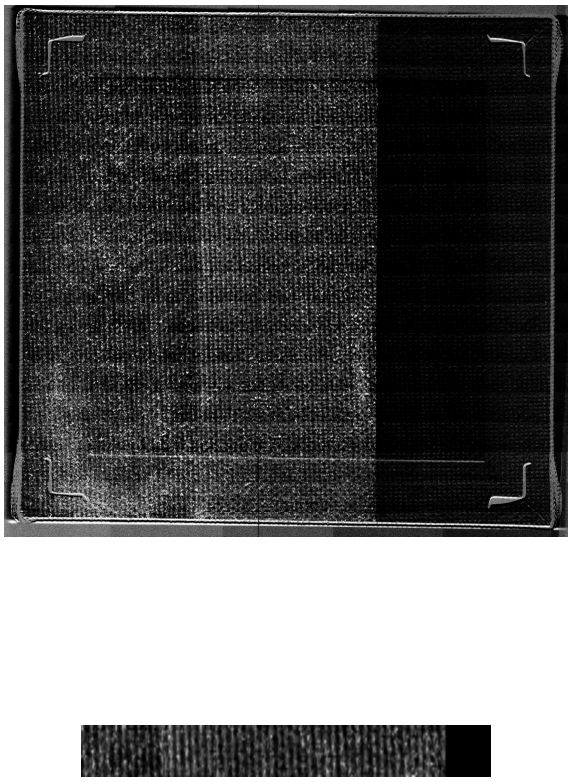

Figure 5.23: Mapping with CCD and SSD of Arsenic distribution: the As compound is on the left part of the sample

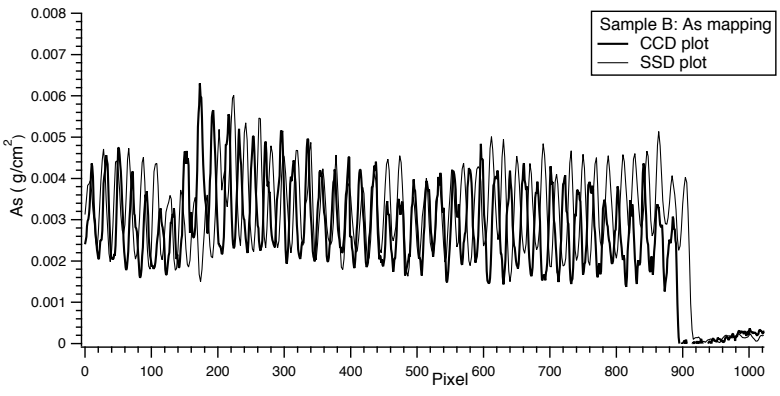

Figure 5.24: Average Arsenic content by column obtained on all SSD map and the corresponding region on CCD image

Figure 5.25: Mapping with SSD of Cadmium distribution: the Cd compound is on the right part of the sample

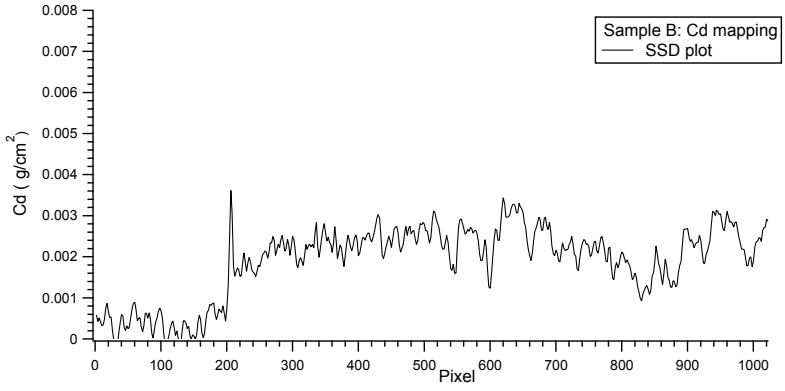

Figure 5.26: Average Cadmium content by column obtained on SSD map

5.9 Paintings

K-edge radiography to investigate Zinc distribution has been also applied to a test painting and to paintings on canvas and on thin wood. In the next sections obtained results will be show.

5.9.1 Test Painting

A test painting (Fig.5.27[a]) has been realized using on the left hand Zinc, Cadmium, Chromium and Cobalt pigments and, on the other side, organic pigments only. In Fig.5.27[b,c] the CCD and SSD Zinc mapping are shown. A higher Zn content is detected in the left part of the painting. Unexpected Zinc has been detected in the right part where only organic pigments have been used.
This was explained by XRF analysis, which highlighted Zn, Cd, Cr and Co content in the left side (Fig.5.29[a]) but also a Zinc content used for the canvas preparation on the right part of the painting (Fig.5.29[b]).
Also a Cadmium mapping with SSD detector, of a small area in the middle part of the painting, has been performed. It is shown in Fig.5.28.

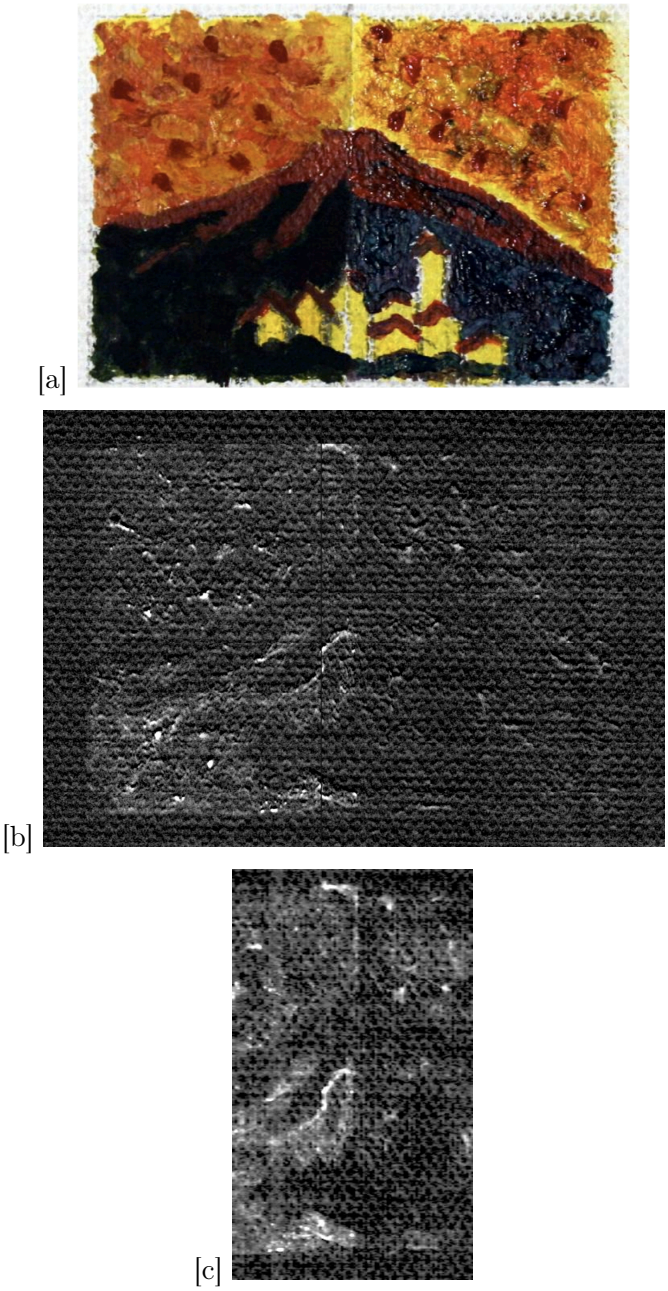

Figure 5.27: Zinc mapping of painting [a] with CCD [b] and SSD [c] detectors.

[a]

[b]

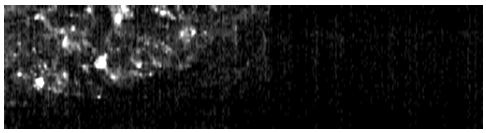

Figure 5.28: Cadmium mapping of painting [a] with SSD [b].

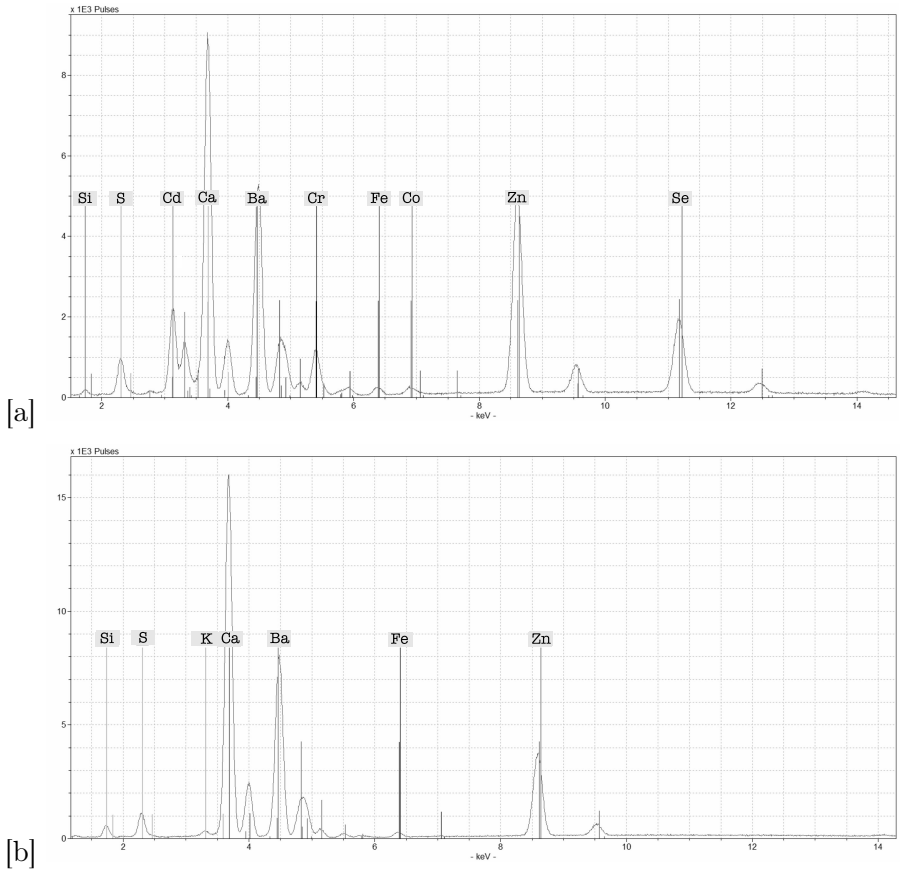

Figure 5.29: XRF analysis on test painting: [a] analysis results on painting layers, [b] analysis on canvas where Zinc presence is highlighted.

5.9.2 La moisson a Montfoucault

K-edge radiography has been performed on a small oil painting on canvas, "La moisson a Montfoucault" (Fig.5.30[a]), a copy from Pissarro, 1980.
The whole painting surface (about 20× 30 cm) has been scanned by CCD detector. A preliminary XRF analysis of the canvas has been performed to confirm the presence of Zinc white and the absence of Lead white.
Measurements were done with the same energies, KVp and current settings of other Zinc analysis (5.4).
The Zinc distribution obtained is shown in Fig.5.30[b]. As can be observed, the Zinc content of the painting can be clearly differentiated: Zn pigments have been used to paint the sky, the wheat (lower side of the picture) and several points of the tree.

[a]

[b]

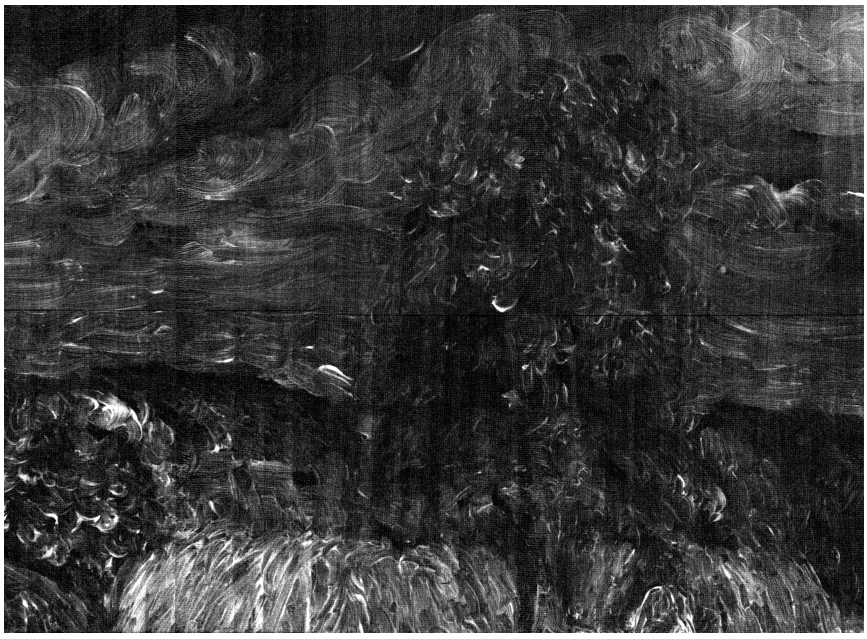

Figure 5.30: "La moisson a Montfoucault", Oil on canvas, 1980, detail comparison between visible light and K-edge radiography on Zn obtained.

5.9.3 "Landscape"

K-edge analysis has been performed on a small painting on a thin wooden panel, "Landscape", XX century.
The middle part of the painting surface has been analyzed.
Same energies, KVp and current settings of the previous analysis have been used.
Zinc mapping confirmed the presence of Zinc in the whole detail (Fig.5.31).
Lighter regions of the image should indicate higher Zinc content.
However thick brushstrokes in the center part of the image appear darker, although the Zinc content is higher. This artifact is due to an excessive attenuation of the X-ray beam. Too low photon flux makes the Lehmann algorithm to fail.

Figure 5.31: Landscape on wood, Zinc mapping obtained

5.9.4 "Sea landscape"

Another small painting on a thin wooden panel, "Sea landscape", has been analyzed, where brushstrokes are not so heavy.
Same energies, KVp and current settings of the previous analysis have been used.
Zinc mapping highlighted the presence of Zinc in the sky, in the sea and in the brushstrokes on the ship with no artifact (Fig.5.32).

Figure 5.32: Sea landscape on wood, analyzed detail with K-edge radiography on Zinc

Chapter 6

Other X-rays applications

Digital radiography allows an higher gray level range than traditional radiography on silver halide plates.
At the Larix Laboratory (Department of Physics, Ferrara University)a X-ray scanner to perform digital radiography of great dimension painting has been designed and realized.
The system may be disassembled and move to perform X-ray scan *in situ*.

6.1 X-ray Scanner

The X-ray scanner is shown in figure 6.1.
The device has been designed to prevent unnecessary movements of the painting. It is positioned and fixed between X-ray source and detector. The both are moving synchronous during a scan.
The dimensions, 2.6×2.30×1 m allow to perform X-ray diagnostics on paintings up to 2.5×1.5 m. X-ray source used is a mammographic X-ray tube, Varian M147 [1], with rotating Tungsten anode and 0.63 mm Beryllium window. The X-ray tube is powered by a high-frequency, high-voltage generator [2], 40 KVp max achievable.
To perform digital radiography a Flat Panel Sensor C7930DK by Hamamatsu [3] is used.
It is a great dimensions CMOS detector, 220.8×176 mm with 4384×3520 pixels, pitch $50\mu m$ and 12-bit digital output.
The X-ray tube and the detector are mounted specularly on an double aluminum arm. This setup provides the best detector-source stability.
Arm movements are performed with two motorized scanning system, one for each directions x and y. All the scanning systems and detector acquisition process are remote controlled by dedicated pc. A commercial software, PTGui [4], is used off-line to merge single images obtained.

[1] Varian Medical System, Inc., Palo Alto, U.S.A
[2] Metaltronica Srl, Roma, Italy
[3] Hamamatsu Photonics K.K., Japan
[4] Software by New House Internet Service B. V., Rotterdam, The Netherlands

[a] 

[b] 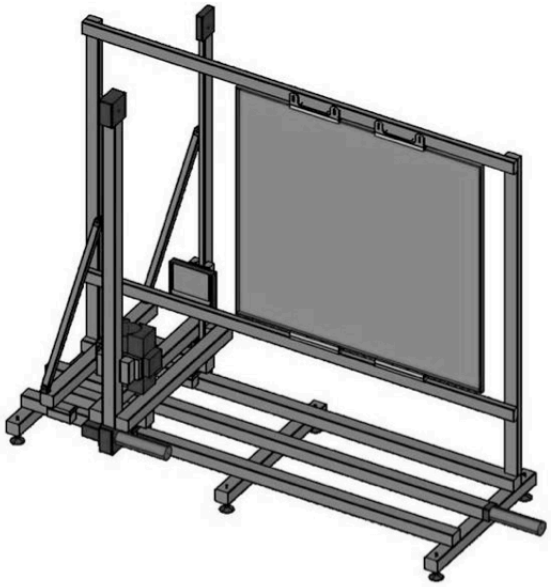

Figure 6.1: X-ray scanner facility

6.2 Some application of X-ray digital radiography of paintings

6.2.1 Landscape, wooden panel, XX cent.

Due to the small size of the painting, 45 cm diamater, only six radiographic images have been acquired.
As explained in chapter 1.4, dark current and white field image corrections have been done.
The result, after correction and merging is presented in Fig.6.2[b].
An underpainting, a woman portrait, is now visible.
Traditional radiography on X-ray films, to investigate paintings
composed of several material with great different absorption coefficients, needs to perform several sets of radiographies using different KVp settings.
The gray level range by 12-bit digitalization allows to acquire only one image. The visualization of all detail of the painting is performed by changing contrast and luminosity settings.
The low-absorber outer edge of the paintings, probably made of leather or cardboard, became visible (Fig.6.3[a]).
By the same way, nails inside the support are highlighted, as shown in Fig.6.3[b].

[a]

[b]

Figure 6.2: Anonymous, “Landscape”, Oil on wood, XX century.
Comparison between visible light and X-ray radiography

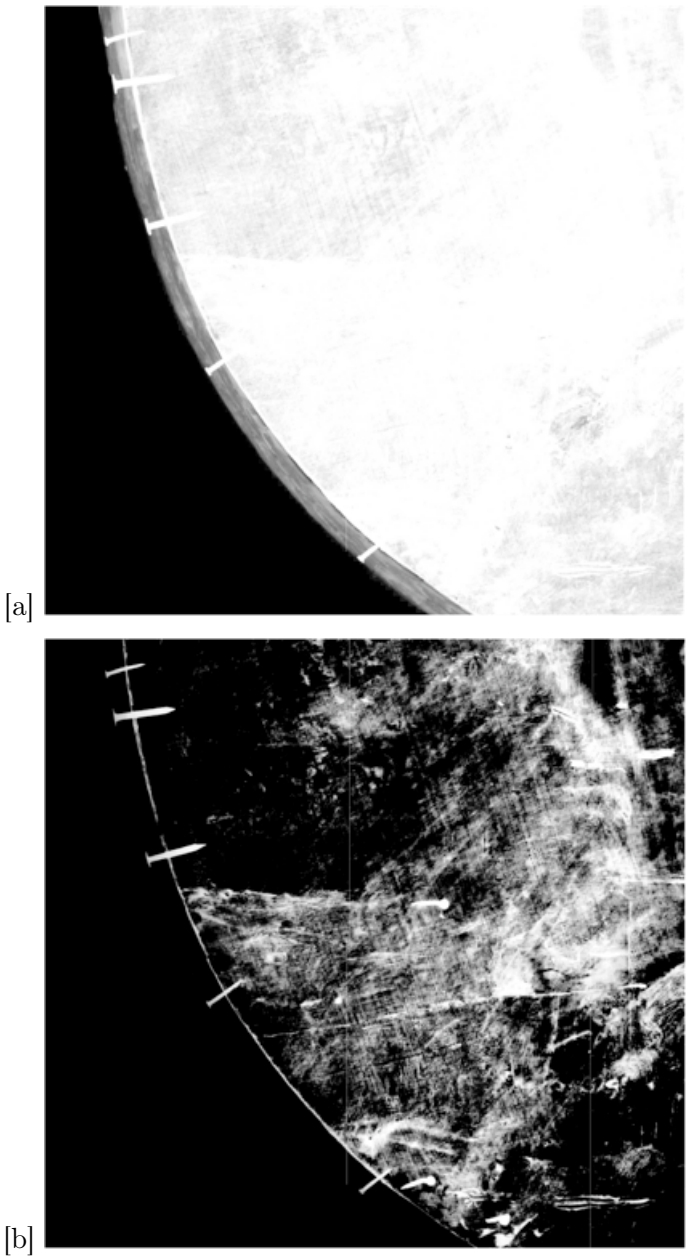

Figure 6.3: Analyzed detail; [a] the low-absorber outer edge and [b] nails inside the support

6.2.2 Wooden Crucifix

Digital X-ray radiography has been used to analyze a small wooden sculpture, a processional crucifix of XVIII century.
A single radiographic image is show in (Fig.6.4). A different wood type used for body and hair is evident. Nails to hold the crown of thorns have been discovered.
In head detail and entire radiography (Fig.6.5) several restoration problems are emphasize.
Iron pins inside shoulder are seem and in the same area a low-absorption material is used, probably glue to solidate binders and fill the damage part. Same material seems used for knees and feet deficiencies.

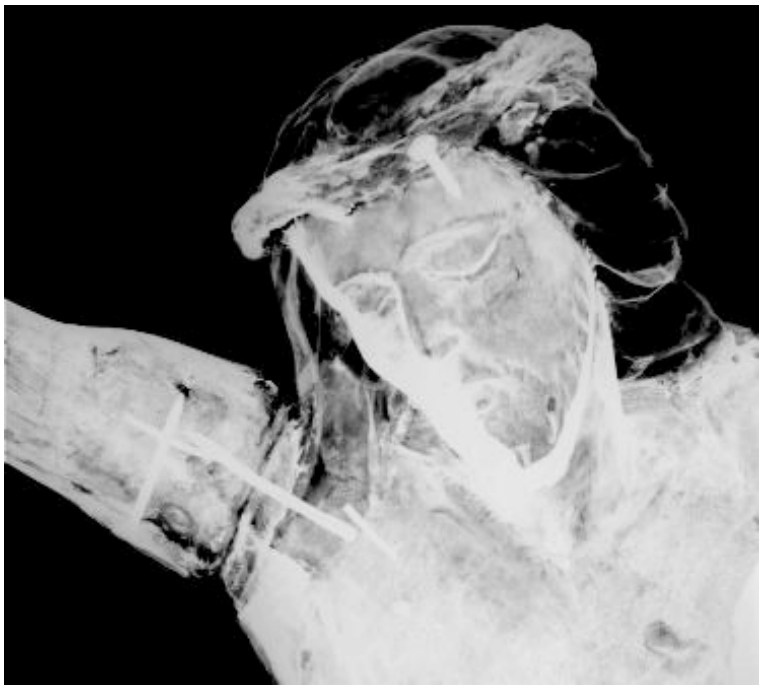

Figure 6.4: Anonimous, wooden Crucifix, XVIII century. X-ray radiography of Crucifix head detail

Figure 6.5: Anonimous, wood Crucifix, XVIII century. X-ray mosaic of entire sculpture

6.2.3 "Maddalena penitente", oil on canvas, XVIII cent.

Due to the painting size, about 95×120 cm, 45 radiographic images have been acquired and the final merge is shown in Fig.6.7.
Restoration are highlighted and old damages on all painting surface are now visible.

Figure 6.6: Anonymous, "Maddalena penitente", Oil on canvas, XVIII century. Visible light

Figure 6.7: Anonymous, "Maddalena penitente", Oil on canvas, XVIII century. X-ray radiography.

Chapter 7

Conclusions

In this work a quasi-monochromatic X-ray system for K-edge imaging in art pigments has been described and characterized.
Beams in the energy range 7-40 KeV have been analyzed, at the energies of K-edge of Iron, Copper, Cobalt, Zinc, Arsenic, Bromine, Strontium, Molybdenum, Silver, Cadmium Tin and Barium.
Beams have a good degree of monochromatization and the system shown a relatively high monochromatization efficiency.
Monochromatic beams with higher flux have been produced in the energy range which includes anode emission peaks, K_α=17.48 KeV and K_β=19.61 KeV.
Due to this increasing flux a great dissimilarity from Low and High image signals occur. Analysis of elements with K-edge in this range (Strontium and Molybdenum) can be more difficult.
Despite of good characteristics of the produced beams, the use of traditional X-ray source implies a low total flux.
A low KVp is necessary to prevent second order diffraction and, in particular at lower energies, air attenuation reduces strongly the photon flux. This can prevent use of this facility to perform elemental mapping on wood paintings or on painting with thick brushstrokes. An helium box to include K-edge facility can increase photon flux.
K-edge mapping has been successfully tested with different detectors, a commercial CCD and a SSD and a fairly good quantitative correspondence. SSD present an higher efficiency at energies above 20 KeV, CCD detector allows faster acquisition due to the large detection area.
K-edge imaging has been successfully tested in the detection of different elements (from Iron to Tin) on pigment samples and on test paintings.

Bibliography

[1] A. Gilardoni, R. Ascani Orsini, S. Taccani
X-Rays in Art (Gilardoni, Mandello Lario, 1994)

[2] M. Milazzo, C. Cicardi
Archaeometry 40, 351 (1998)

[3] P.A. Mandó, M.E. Fedi, N. Grassi, A. Migliori
Nucl. Instrum. Methods B 239, 71 (2005)

[4] L.A. Lehmann, R.E. Alvarez, A. Macovski, W.R. Brody
Med. Phys. 8(5), 659 (1981)

[5] A. Sarnelli, H. Ellaume, A. Taibi, M. Gambaccini, A. Bravin
Phys. Med. Biol 51, 4311-4328, (2006)

[6] P. Baldelli, A. Bravin, C. Di Maggio, G. Gennaro, A. Sarnelli, A. Taibi, M. Gambaccini
Phys. Med. Biol 51, 4233-4251, (2006)

[7] R. Lewis
Phys. Med. Biol. 42, 1213 - 1243 (1997)

[8] P. Baldelli, A. Taibi, A. Tuffanelli, M.C. Gilardoni,
M. Gambaccini
Phys. Med. Biol. 50, 2225 (2005)

[9] P. Baldelli, L. Bonizzoni, M. Gambaccini, M. Gargano,
N. Ludwig, M. Milazzo, L. Pasetti, P. Petrucci, F. Prino,
L. Ramello, M. Scotti
Nuovo Cimento 29, 663-672 (2006)

[10] K. Krug, J. Dik, M. Den Leeuw, A. Whitson, J. Tortora, P. Coan, C. Nemoz, A. Bravin
Appl. Phys. A 83, 247 (2006)

[11] Chimica per l'arte L.Campanella *et. al*
2007 Zanichelli-Bologna

[12] Pigments through the Ages
http://www.webexhibits.org/pigments

[13] Kremer Pigmente Data Sheets

[14] A. K. Freund
Nucl. Instrum. Methods, A266, 461(1988)

[15] M. Ohler, M. Sanchez Del Rio, A. Tuffanelli, M. Gambaccini, A. Taibi, A. Fantini, G.J. Pareschi
Appl. Cryst. 33, 1023 - 1030 (2000)

[16] NIST XCOM: Photon Cross Sections Database
http://www.nist.gov/physlab/data/xcom/index.cfm

[17] A. Sarnelli, C. Nemoz, H. Elleaume, F. Esteve, B. Bertrand, A.Bravin
Phys. Med. Biol. 50, 725 (2005)

[18] Amptek, XR-100T-CZT Detector Datasheet

[19] A. Sarnelli, A. Taibi, A. Tuffanelli, G. Baldazzi, D. Bollini, A. E. Cabal Rodriguez, M. Gombia, F. Prino, L. Ramello, E. Tomassi, M. Gambaccini
Phys. Med. Biol. 49, 3291-3305, (2004)

[20] L. Ramello, F. Prino, P. Grybos, P. Maj, K. Swientek, R. Szczygiel, L. Bolanos, A. E. Cabal, F. Petrucci, M. Gambaccini, F. Albertin
European Federation of Organisations for Medical Physics, EFOMP Congress - Pisa 20-22 Sept. 2007 - Poster Session P3-17

[21] Hamamatsu - Technical information SD-25
Characteristics and use of FFT-CCD area image sensor

[22] http://www.photometrics.com

Your E-Mail Address
fauzia.albertin@student.unife.it
Subject
dichiarazione di conformità tesi
Io sottoscritto Dott. (Cognome e Nome)
Albertin Fauzia
nato a
Bologna
Provincia
Bologna
il giorno
25/08/1981
avendo frequentato il corso di Dottorato di Ricerca in:
Fisica
Ciclo di Dottorato
XXIII
Titolo della tesi in Italiano
Radiografia differenziale al K-edge e applicazioni per i beni culturali
Titolo della tesi in Inglese
K-edge radiography and applications to Cultural Heritage
Titolo della tesi in altra Lingua Straniera
Tutore - Prof:
Gambaccini Mauro
Settore Scientifico Disciplinare (SSD)
Fis 07
Parole chiave (max 10)
Raggi X, radiografia, Beni Culturali, X-ray, radiography, K-edge, Cultural Heritage
Consapevole - Dichiara
CONSAPEVOLE --- 1) del fatto che in caso di dichiarazioni mendaci, oltre alle sanzioni previste dal codice penale e dalle Leggi speciali per l'ipotesi di falsità in atti ed uso di atti falsi, decade fin dall'inizio e senza necessità di alcuna formalità dai benefici conseguenti al provvedimento emanato sulla base di tali dichiarazioni; -- 2) dell'obbligo per l'Università di provvedere al deposito di legge delle tesi di dottorato al fine di assicurarne la conservazione e la consultabilità da parte di terzi; -- 3) della procedura adottata dall'Università di Ferrara ove si richiede che la tesi sia consegnata dal dottorando in 4 copie di cui una in formato cartaceo e tre in formato .pdf, non modificabile su idonei supporti (CD-ROM, DVD) secondo le istruzioni pubblicate sul sito : http://www.unife.it/dottorati/dottorati.htm alla voce ESAME FINALE – disposizioni e modulistica; -- 4) del fatto che l'Università sulla base dei dati forniti, archivierà e renderà consultabile in rete il testo completo della tesi di dottorato di cui alla presente dichiarazione attraverso l'Archivio istituzionale ad accesso aperto "EPRINTS.unife.it" oltre che attraverso i Cataloghi delle Biblioteche Nazionali Centrali di Roma e Firenze. --- DICHIARO SOTTO LA MIA RESPONSABILITA' --- 1) che la copia della tesi depositata presso l'Università di Ferrara in formato cartaceo, è del tutto identica a quelle

presentate in formato elettronico (CD-ROM, DVD), a quelle da inviare ai Commissari di esame finale e alla copia che produrrò in seduta d'esame finale. Di conseguenza va esclusa qualsiasi responsabilità dell'Ateneo stesso per quanto riguarda eventuali errori, imprecisioni o omissioni nei contenuti della tesi; -- 2) di prendere atto che la tesi in formato cartaceo è l'unica alla quale farà riferimento l'Università per rilasciare, a mia richiesta, la dichiarazione di conformità di eventuali copie; -- 3) che il contenuto e l'organizzazione della tesi è opera originale da me realizzata e non compromette in alcun modo i diritti di terzi, ivi compresi quelli relativi alla sicurezza dei dati personali; che pertanto l'Università è in ogni caso esente da responsabilità di qualsivoglia natura civile, amministrativa o penale e sarà da me tenuta indenne da qualsiasi richiesta o rivendicazione da parte di terzi; -- 4) che la tesi di dottorato non è il risultato di attività rientranti nella normativa sulla proprietà industriale, non è stata prodotta nell'ambito di progetti finanziati da soggetti pubblici o privati con vincoli alla divulgazione dei risultati, non è oggetto di eventuali registrazioni di tipo brevettale o di tutela. --- PER ACCETTAZIONE DI QUANTO SOPRA RIPORTATO

Firma Dottorando

Ferrara, lì _____ Firma del Dottorando

_____

Firma Tutore

Visto: Il Tutore Si approva Firma del Tutore _____